ELSEVIER

International Journal of Solids and Structures 41 (2004) 1173–1208

INTERNATIONAL JOURNAL OF SOLIDS and STRUCTURES

www.elsevier.com/locate/ijsolstr

# Spectral finite element analysis of coupled wave propagation in composite beams with multiple delaminations and strip inclusions

D. Roy Mahapatra, S. Gopalakrishnan *

*Department of Aerospace Engineering, Indian Institute of Science, C.V. Raman Road, Bangalore 560012, India*

Received 15 October 2003; received in revised form 15 October 2003

**Abstract**

A spectral finite element model (SFEM) is developed to study the effect of wave scattering and power flow through multiple delaminations and strip inclusions in composite beams with general ply stacking sequence. The model uses three dimensional beam waveguides to represent the dynamics of the base-laminates and the sub-laminates or strip inclusions with distributed friction at the interlaminar region. A compact matrix methodology based on finite element discretization in wavenumber space ($k$-space) and fast Fourier transform (FFT) to obtain frequency domain as well as time domain response is developed. This model has exact shape function and dynamic stiffness matrices, and dynamically consistent load vector, which can be used to analyze broadband coupled wave propagation in composite beam waveguide. In the present paper, a sub-laminate-wise constant shear kinematics with multi-point constraints (MPC) in frequency domain is used to model the interface between multiple delaminations or strip inclusions and the base-laminate. The strip inclusion, which can be a passive or active device or integrated electronics embedded inside laminated composite, are considered to be in the form of rectangular sub-laminates with different material properties compared to the host structure. Performance of the model is validated by comparing the response from 2D plane stress finite element solution. Effect of length-wise and depth-wise multiple delaminations and strip inclusion on the scattered power flow is studied. The analysis may find its suitability and superiority to capture the dynamics of delaminated composite structure over broad frequency band in vibrating environment and in structural health monitoring applications using diagnostic waves.


*Keywords:* SFEM; FFT; Wavenumber; Multiple; Delaminations; Strip inclusion; Power flow; Scattering; Interface; Bounded media; Distributed contact

* Corresponding author. Tel.: +91-080-2933019/3943019; fax: +91-080-3600134.
*E-mail address:* krishnan@aero.iisc.ernet.in (S. Gopalakrishnan).

0020-7683/$ - see front matter © 2003 Elsevier Ltd. All rights reserved.
doi:10.1016/j.ijsolstr.2003.10.018

## 1. Introduction

Extensive tailorability of the fiber reinforced laminated composite and thin film type layered structures have lead to present day's state of the art in smart structures and micro-electro-mechanical systems (MEMS). Such structures are potential candidates for specific and complex applications due to their multi-functionality. From the view-point of mechanical performance, very high stiffness-to-weight ratio is one of the well exploited functionality. There are also special structural designs of interest, where the effect of stiffness coupling is used for flextensional and shear induced actuation and shape (Senthil and Batra, 2001). Also, for smart structural applications, laminated composite structures can be designed as the host structures with a diverse range of micro-sensors and actuators and even the entire electronics (Heschel et al., 1998) embedded in them. In recent days, there are many other application of laminated composite materials, such as active control of sound (Cai et al., 2001) etc., which are of less structural importance and are fabricated to meet multi-physics requirements in micro-electro-mechanical (MEMS) devices, integrated circuits operating at extreme environment.

Delamination and debonding of devices embedded in laminated composite structure is one of the crucial mode of damages (Luo and Hanagud, 2000; Tsai et al., 2001; Tong et al., 2001). When such an integrated heterogeneous system is exposed to highly transient dynamic or fatigue loading, for example in flexbeam of helicopter rotor-blades (Purekar and Pines, 2000), multiple waves in the low to high frequency ranges are generated. At minute interfaces between heterogeneous stiffness and mass systems, considerable change in the nearfield effects may occur due to scattering of waves. One crucial outcome of such phenomena is the dynamic stress intensity at the delaminations tips (Chakraborty et al., 2001). This may enhance the formation of delamination in the locations of severe stress discontinuities. Especially, modern composite structures with several embedded micro-devices need special treatment based on simulation at the design stage. Further, for an operational composite structures, health monitoring becomes an important issue due to high cost of obtaining test data and its post-processing to identify the delaminated or debonded configuration in interior locations. To address such issues in the context of structural health monitoring software and systems, wave based diagnostics and related modeling complexities have been discussed in several literature (Doyle, 1995; Lakshmanan and Pines, 1998; Purekar and Pines, 2000; Park et al., 2000; Kessler et al., 2002; Nag et al., 2002). Several defects and composite material aging effect changes the characteristic structural behaviour. Also, non-ideal boundaries and finite geometry make model based predictions difficult to match with the test data. To alleviate such difficulty, one may seek most of the numerical analysis data to be in the form of digital signals. In this paper, we take the advantage of fast Fourier transform (FFT) algorithm coupled with Finite Element (FE) analysis to solve the wave propagation and its interaction with the delaminations and debonding of strip inclusions embedded inside laminated composite.

In most of the real life situations, it is observed that one or more delaminations across the thickness of the laminated structure produce membrane-flexural–torsional coupling. Therefore, even in the presence of only in-plane or torsional loading, flexural waves are generated which are dispersive in nature. As the total thickness increases, additional shear waves and then higher order antisymmetric and symmetric Lamb wave modes become dominant with wave speeds exceeding the in-plane wave speed. This implies that the modeling of delaminated configuration in conventional FE analysis to capture the propagating stress waves, very fine mesh is required. Also, the delamination tips may need further mesh refinements, which make efficient analysis of the global behaviour very difficult.

On the other hand, in the modeling approaches based on wave propagation, it is possible to identify the presence of damage using certain simplified assumptions such as equivalent material degradation (Park et al., 2000) at the crack or delamination interface. Such a model influence a changes in the speeds of different wave modes (longitudinal, flexural, shear) and hence the wavenumbers associated with those modes. In another approach (Lakshmanan and Pines, 1998; Purekar and Pines, 2000), where a set of

scattering matrices are derived based on reflection and transmission of incident waves at structural boundaries, the phase change due to presence of damage at different frequencies can be used to quantify the damage. However, here one needs a sensor and an actuator confining the damage, and then use a controller to cancel the resonances and antiresonances due to structural boundaries through a dereververated transfer function (DTF). Also, in the above approaches, detail model of delamination or debonding and hence scattering of coupled waves at and inside the damage cannot be incorporated. Also, these analytical models are limited by the possibility of algebraic manipulation in closed form, which is often very cumbersome while dealing with axial–flexural–shear coupled wave propagation in composite structures. Since, most of the analytical formulations available in the literature are based on isotropic material configuration with symmetrically placed single damage model, a general framework needs to be explored considering multiple delaminations and debonding of inclusions.

In continuum mechanics formulation for damage or inclusion, one can use a mixed variational formulation in the local model to capture the localized stress field accurately. An assumed stress field for the local damage region and assumed displacement for the global region can generally be used (Pagano, 1989). Here, one can consider an appropriate damage dependent constitutive model (Coats and Harris, 1995) based on continuum damage mechanics for the local region, and equivalent fiber–matrix mixture constitutive model (Reddy, 1997) for the global region. However, such detail model becomes computationally intensive in the context of structural health monitoring and identification of damage using model based prediction and diagnostic wave propagation. In such problems, the available simplified distributed parameter approach is to neglect the relative rotation of the damaged and undamaged sections (in case of beams and plates) and treat the structures with the Euler–Bernoulli (in case of beam) and Kirchhoff (in case of plates) type kinematics. Such models have been verified experimentally in Purekar and Pines (2000) in the context of wave propagation in delaminated isotropic helicopter flexbeams, and in Luo and Hanagud (2000) in the context of natural frequency change in first order shear deformable composite beam with delamination and the associated contact non-linearity in the low frequency dynamics. Also, such simplified model can be found useful while modeling advanced composite with stitching (Sankar and Zhu, 2000) and various other types of material interfaces. Considering axial–flexural–shear coupled wave propagation in composite beams, a damaged spectral element has been developed in Nag et al. (2002), where exact dynamics of internal debonded sub-laminates are also taken into account. This formulation then condense out the FE nodal information of the internal waveguides, and hence allows one to replace an undamaged composite beam segment with this damaged spectral element where delamination exists. Such formulation is based on the spectral finite element model (SFEM), which is also used but in a more general framework in the present study. Although the reported models, e.g. Luo and Hanagud (2000) and Nag et al. (2002) uses constant rotation of the interface between the damaged and undamaged segments, these are not capable of capturing the differential rotation of individual debonded sub-laminates at their interfacial cross-section with the base-laminates. This is also an important effect to consider for thickness-wise multiple delaminations or other forms of damage and inclusion. This restriction due to constant shear kinematics can be eliminated using the approach reported in Barbero and Reddy (1991), where the layer-wise kinematics allows individual sub-laminates to rotate by different amounts. Similar approach has been used in Kouchakzadeh and Sekine (2000), where the formulation uses penalty function to impose appropriate constraints at the interface between base-laminates and multiple sub-laminates. In the works of Lee et al. (1993) and Lee (2000), the interface is assumed to translate and rotate in a rigid body mode. Thus, the normal plane is assumed continuous across the base-laminate thickness and is hence not affected by the stress discontinuity in the two delaminated faces at the tip due to Mode-I and Mode-II stable delaminations. However, this assumption may not be adequate, since strong coupling between the displacement components may exist in case of asymmetric ply stacking, asymmetry among the sub-laminates (due to inclusions of different materials) and discontinuity in the stiffness and inertia by foreign inclusions such as MEMS devices and integrated electronics.

Models based on 2D elastodynamics is the ideal candidate for wave propagation in cracked beam problems under plane stress or plane strain condition. Spectral analysis of such semi-infinite domain containing crack has been studied by many researchers (e.g. Geubelle and Rice, 1995; Liu and Achenbach, 1995). The strip element method for wave scattering in cracked composite was first proposed by Liu and Achenbach (1995). The strip element method uses the characteristic solution (wavenumber dispersion) of the 2D elastodynamic equation and eigenvectors to compute the displacement in terms of integral expression. This method was later extended by Xi et al. (2000) for analyzing wave scattering by an axisymmetric crack in a laminated composite cylindrical shell filled with fluid under axisymmetric configuration. A hybrid method by combining finite element discretization in propagation direction and strip element discretization in thickness direction in cracked laminates was developed by Liu (2002). A spectral super-element model was used by Gopalakrishnan and Doyle (1995) to model transverse crack in isotropic beam and the dynamic stress intensity factor was obtained accurately under impact type loading.

The spectral element technique used in Nag et al. (2003) to model horizontal crack or delamination in laminated composite beam was based on interface kinematics between the sub-laminates and the base-laminate. In the present paper, displacement-based spectral finite elements are derived for coupled wave propagation in general laminated composite beam with 3D anisotropic constitutive model and higher order inertia. The coupled wave equations which are essentially PDEs in space and time are transformed into Fourier domain using discrete Fourier transform (DFT). Next, the exact shape function matrix, strain–displacement matrix and dynamic stiffness matrix are formed in wavenumber space ($k$-space). Finite element assemblage is used to finally form the SFEM. Treatment of different types of boundary constraints within this framework of SFEM are discussed. Although the computational complexity remains nearly of same order as in conventional FE model with very large system size, only one spectral element is sufficient to model a uniform or tapered beam segment. Thus, the computer storage requirement in SFEM is many order smaller compared to the conventional FEM. This also improve the speed of computation while system solving and post-processing the result. In the present work, we extend the same concept to model the individual sub-laminates or strip inclusions. A layer-wise constant shear kinematics is then imposed at the interfaces of sub-laminates and base-laminates at their interfaces. Equilibrium of the discretized system is obtained using multi-point constraints (MPC) in Fourier domain associated with the nodal displacement components and the force components at these interfaces. This allows us to model small local rotations of the individual sub-laminates and the base-laminates at the interface in an average sense. Also, the model is a general one, where the length-wise multiple delaminations of debonding between strip inclusions can be modeled easily. Another advantage of the proposed model is that both the frequency domain changes in phase and amplitude of scattered waves in presence of delaminations or strip inclusions as well as the time domain change in the response can be computed efficiently with the help of FFT (Mahapatra et al., 2001b).

In the present paper, the behaviour of spectral power flow is discussed, which is then used to construct a measure of scattered power in terms of the healthy structure and structures with delaminations and strip inclusions. Since, the model allows one to consider multiple scattering of broadband waves from structural boundaries, it is possible to use direct frequency domain or time domain signal measurements, without the use of any controller to cancel the resonances and antiresonances due to structural boundaries, and to quantify the effect of delaminations of strip inclusions from the view-point of energy transmission capacity (power flow). In the numerical simulations, the scattered power measure is used to quantify the effect of length-wise as well as depth-wise multiple delaminations and strip inclusions. Using the proposed model, single or multiple strip inclusions in the form of rectangular sub-laminates with different material properties can be analyzed. Effect of distributed friction at the interlaminar region (between the host sub-laminates and the strip inclusions) are also considered. Such a model can also be used to identify any material degradation at a local level inside laminated composite structures.

## 2. Linear wave motion in laminated composite beams

We consider the first order shear flexible displacement field given by

$$u(x,y,z,t) = u^0(x,t) + y\theta_z(x,t) + z\theta_y(x,t), \tag{1a}$$

$$v(x,y,z,t) = v^0(x,t) - z\theta_x(x,t), \tag{1b}$$

$$w(x,y,z,t) = w^0(x,t) + y\theta_x(x,t), \tag{1c}$$

where $u^0$, $v^0$, $w^0$, $\theta_x$, $\theta_y$ and $\theta_z$ are the longitudinal displacements, the transverse and lateral displacements, and the cross-sectional rotations about the reference $(X, Y, Z)$ axis system. The above form provides three displacement and three rotational degrees of freedom at any material point as functions of length $x$ along the beam axis (Fig. 1). The constitutive model for anisotropic composite in global $(X, Y, Z)$ coordinate system can be expressed as

$$\begin{Bmatrix} \sigma_{xx} \\ \tau_{xz} \\ \tau_{xy} \end{Bmatrix} = \begin{bmatrix} \overline{C}_{11} & \overline{C}_{15} & \overline{C}_{16} \\ \overline{C}_{15} & \overline{C}_{55} & \overline{C}_{56} \\ \overline{C}_{16} & \overline{C}_{56} & \overline{C}_{66} \end{bmatrix} \begin{Bmatrix} \varepsilon_{xx} \\ \gamma_{xz} \\ \gamma_{xy} \end{Bmatrix}. \tag{2}$$

Using Hamilton's principle, the six wave equations in homogeneous form (excluding the effect of distributed force) are obtained as

$$\begin{aligned} &\delta u^0 : 0 \\ &= M_{11}\ddot{u}^0 + M_{13}\ddot{\theta}_y + M_{12}\ddot{\theta}_z - A_{1111}u^0{}_{,xx} - A_{1611}v^0{}_{,xx} - A_{1511}w^0{}_{,xx} + (A_{1613} - A_{1512})\theta_{x,xx} \\ &\quad - A_{1113}\theta_{y,xx} - A_{1112}\theta_{z,xx} - A_{1511}\theta_{y,xx} - A_{1611}\theta_{z,x}, \end{aligned} \tag{3a}$$

$$\begin{aligned} &\delta v^0 : 0 \\ &= M_{11}\ddot{v}^0 - M_{13}\ddot{\theta}_x - A_{1611}u^0{}_{,xx} - A_{6611}v^0{}_{,xx} - A_{5611}w^0{}_{,xx} + (A_{6613} - A_{5612})\theta_{x,xx} - A_{1613}\theta_{y,xx} - A_{1612}\theta_{z,xx} \\ &\quad - A_{5611}\theta_{y,x} - A_{6611}\theta_{z,x}, \end{aligned} \tag{3b}$$

$$\begin{aligned} &\delta w^0 : 0 \\ &= M_{11}\ddot{w}^0 + M_{12}\ddot{\theta}_x - A_{1511}u^0{}_{,xx} - A_{5611}v^0{}_{,xx} - A_{5511}w^0{}_{,xx} + (A_{5613} - A_{5512})\theta_{x,xx} - A_{1513}\theta_{y,xx} - A_{1512}\theta_{z,xx} \\ &\quad - A_{5511}\theta_{y,x} - A_{5611}\theta_{z,x}, \end{aligned} \tag{3c}$$

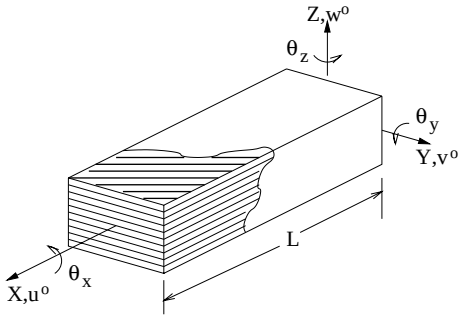


Fig. 1. Degrees of freedom in the 3D composite beam.

$$\delta\theta_x : 0$$
$$= (M_{22}+M_{33})\ddot{\theta}_x - M_{13}\ddot{v}^0 + M_{12}\ddot{w}^0 + (A_{1613}-A_{1512})u^0{}_{,xx} + (A_{6613}-A_{5612})v^0{}_{,xx} + (A_{5613}-A_{5512})w^0{}_{,xx} + (2A_{5623}-A_{5522}-A_{6633})\theta_{x,xx} + (A_{1633}-A_{1523})\theta_{y,xx} + (A_{1632}-A_{1522})\theta_{z,xx} + (A_{5631}-A_{5521})\theta_{y,x} + (A_{6631}-A_{5621})\theta_{z,x}, \tag{3d}$$

$$\delta\theta_y : 0$$
$$= M_{33}\ddot{\theta}_y + M_{13}\ddot{u}^0 + M_{23}\ddot{\theta}_z - A_{1113}u^0{}_{,xx} - A_{1613}v^0{}_{,xx} - A_{1513}w^0{}_{,xx} + (A_{1633}-A_{1523})\theta_{x,xx} - A_{1133}\theta_{y,xx} - A_{1123}\theta_{z,xx} + A_{1511}u^0{}_{,x} + A_{5611}v^0{}_{,x} + A_{5511}w^0{}_{,x} + (A_{5521}-A_{5631})\theta_{x,x} + (A_{1521}-A_{1631})\theta_{z,x} + A_{5511}\theta_y + A_{5611}\theta_z, \tag{3e}$$

$$\delta\theta_z : 0$$
$$= M_{22}\ddot{\theta}_z + M_{12}\ddot{u}^0 + M_{23}\ddot{\theta}_y - A_{1112}u^0{}_{,xx} - A_{1612}v^0{}_{,xx} - A_{1512}w^0{}_{,xx} + (A_{1632}-A_{1522})\theta_{x,xx} - A_{1123}\theta_{y,xx} - A_{1122}\theta_{z,xx} + A_{1611}u^0{}_{,x} + A_{6611}v^0{}_{,x} + A_{5611}w^0{}_{,x} + (A_{5621}-A_{6631})\theta_{x,x} + (A_{1631}-A_{1521})\theta_{y,x} + A_{5611}\theta_y + A_{6611}\theta_z. \tag{3f}$$

Simultaneously, the six force boundary equations in terms of the primary displacement variables can be obtained as

$$N_x = A_{1111}u^0{}_{,x} + A_{1611}v^0{}_{,x} + A_{1511}w^0{}_{,x} + (A_{1512}-A_{1613})\theta_{x,x} + A_{1112}\theta_{z,x} + A_{1113}\theta_{y,x} + A_{1511}\theta_y + A_{1611}\theta_z, \tag{4a}$$

$$V_{xy} = A_{1611}u^0{}_{,x} + A_{6611}v^0{}_{,x} + A_{5611}w^0{}_{,x} + (A_{5612}-A_{6613})\theta_{x,x} + A_{1613}\theta_{y,x} + A_{1612}\theta_{z,x} + A_{5611}\theta_y + A_{6611}\theta_z, \tag{4b}$$

$$V_{xz} = A_{1511}u^0{}_{,x} + A_{5611}v^0{}_{,x} + A_{5511}w^0{}_{,x} + (A_{5512}-A_{5613})\theta_{x,x} + A_{1513}\theta_{y,x} + A_{1512}\theta_{z,x} + A_{5511}\theta_y + A_{5611}\theta_z, \tag{4c}$$

$$M_x = (A_{1512}-A_{1613})u^0{}_{,x} + (A_{5612}-A_{6613})v^0{}_{,x} + (A_{5512}-A_{5613})w^0{}_{,x} + (A_{5522}-2A_{5623}+A_{6633})\theta_{x,x} + (A_{1523}-A_{1633})\theta_{y,x} + (A_{1522}-A_{1632})\theta_{z,x} + (A_{5521}-A_{5631})\theta_y + (A_{5621}-A_{6631})\theta_z, \tag{4d}$$

$$M_y = A_{1113}u^0{}_{,x} + A_{1613}v^0{}_{,x} + A_{1513}w^0{}_{,x} + (A_{1523}-A_{1633})\theta_{x,x} + A_{1133}\theta_{y,x} + A_{1123}\theta_{z,x} + A_{1531}\theta_y + A_{1631}\theta_z, \tag{4e}$$

$$M_z = A_{1112}u^0{}_{,x} + A_{1612}v^0{}_{,x} + A_{1512}w^0{}_{,x} + (A_{1522}-A_{1632})\theta_{x,x} + A_{1123}\theta_{y,x} + A_{1122}\theta_{z,x} + A_{1521}\theta_y + A_{1621}\theta_z. \tag{4f}$$

The overhead dot stands for partial derivative with respect to time and the subscript $\langle{}_{,x}\rangle$ stands for partial derivative with respect to $x$. In the above wave equations (3a)–(3f), and force boundary equations (4a)–(4f), many cross-sectional stiffness and cross-sectional inertial terms appear, which are written respectively using compact matrix notations as

$$\mathbf{A}_{jl} = \int\int \overline{C}_{jl}\boldsymbol{\Psi}^{\mathrm{T}}\boldsymbol{\Psi}\,\mathrm{d}y\,\mathrm{d}z, \quad \mathbf{M} = \int\int \rho\boldsymbol{\Psi}^{\mathrm{T}}\boldsymbol{\Psi}\,\mathrm{d}y\,\mathrm{d}z, \tag{5}$$

where $\boldsymbol{\Psi} = \{\,1 \quad y \quad z\,\}$. Note that in Eq. (5), $\mathbf{A}_{jl}$ is $3\times3$ matrix for each $\overline{C}_{jl}$ and two additional subscripts after $jl$ have been used while expressing single stiffness coefficients in the equations of motion. $\mathbf{M}$ is a $3\times3$ matrix of inertial coefficients. In rest of the paper, small letters in bold faces indicate vectors and capital letters in bold faces represent matrices. The six wave equations (Eqs. (3a)–(3f)) essentially represent space-time coupled PDE, and are not exactly solvable using conventional polynomial shape function approximation in time domain. Hence, in conventional FE approach, appropriate fine mesh and time marching strategy is adopted while solving broadband wave propagation problems.

To alleviate this difficulty under the framework of displacement-based finite element model, we transform the field variables in Fourier domain by forming a set of ODEs. Further, the spatial discretization is carried out in wavenumber space ($k$-space). First, the harmonic solution to the displacement field vector is expressed using discrete Fourier transform (DFT), which is given by

$$\mathbf{u}(x,t) = \sum_{n=1}^{N} \hat{\mathbf{u}}(x,\omega_n)\mathrm{e}^{\mathrm{i}\omega_n t}, \tag{6}$$

where $\hat{(\cdot)}$ represents spectral amplitudes of displacement vector $\hat{\mathbf{u}}(x,\omega_n) = \{\,\hat{u}^0 \quad \hat{v}^0 \quad \hat{w}^0 \quad \hat{\theta}_x \quad \hat{\theta}_y \quad \hat{\theta}_z\,\}^{\mathrm{T}}$ as primary variables along the reference $X$-axis of the beam. $\mathrm{i} = \sqrt{-1}$ and $\omega_n$ is the structural frequency at FFT sampling points and $N$ is the Nyquist point in FFT. In rest of the derivations and discussions, the term spectral amplitude will be assumed while referring to displacements, forces etc. unless stated otherwise, explicitly. Next, the asymptotic spatial variation in $k$-space is considered, which can be written as

$$\hat{\mathbf{u}}(x,\omega_n) = \mathbf{R}\boldsymbol{\Lambda}_0\tilde{\mathbf{u}} = \mathbf{T}_1(x,\omega_n)\tilde{\mathbf{u}}, \tag{7}$$

where $\tilde{\mathbf{u}}_{(12\times1)}$ is the vector of wave coefficients and $\boldsymbol{\Lambda}_0(12\times12)$ is a diagonal matrix with asymptotic entries in characteristic wavenumbers ($k_j,\ j = 1,\ldots,12$), which can be expressed as

$$\Lambda_0 jj = \begin{cases} \mathrm{e}^{-ik_j x} & \text{if } k_j \text{ is } +\text{ve real,} \\ \mathrm{e}^{+ik_j(L-x)} & \text{if } k_j \text{ is } -\text{ve real,} \\ \mathrm{e}^{+ik_j(L-x)} & \text{if } k_j \text{ is } +\text{ve imaginary,} \\ \mathrm{e}^{-ik_j x} & \text{if } k_j \text{ is } -\text{ve imaginary.} \end{cases} \tag{8}$$

Classification of the exponential entries in Eq. (8) is to keep track of propagating and evanescent wave components at each FFT sampling frequencies. In Eq. (7), $\mathbf{R}_{(6\times12)}$ is called amplitude ratio matrix. This is associated with the wave coefficient vector $\tilde{\mathbf{u}}$ and is explained in the formulation of SFEM in Section 3. Each of $k_j$ in Eq. (8) is obtained as root of the 12th order characteristic equation (also called dispersion equation)

$$\mathrm{Det}\,\mathbf{F}(k_j) = 0 \tag{9}$$

obtained by substituting Eqs. (6) and (7) in the wave equations. $\mathbf{F}(k_j)$ is a $6\times6$ complex matrix. Here, it should be noted that closed-form solution to the characteristic equation is very difficult to obtain. Therefore, the wavenumbers are to be computed numerically at each frequency over the frequency window. For symmetric ply stacking configuration, the following form of wavenumbers can be expected as analogous to the isotropic material configuration. There would be a pair of propagating longitudinal waves with wavenumbers

$$k_{1,2} \approx \pm\omega_n\sqrt{\frac{M_{11}}{A_{1111}}}, \tag{10a}$$

a pair of propagating torsional waves with wavenumbers

$$k_{3,4} \approx \pm\omega_n\sqrt{\frac{(M_{22}+M_{33})}{(A_{5522}+A_{6633}-2A_{5623})}}. \tag{10b}$$

There would be a pair of propagating lateral flexural waves and a pair of evanescent lateral shear waves with wavenumbers at low frequencies, respectively, which are given by

$$k_{5,6} \approx \pm\sqrt{\omega_n}\left(\frac{M_{11}}{A_{1122}}\right)^{1/4}, \quad k_{7,8} \approx \pm\mathrm{i}\sqrt{\omega_n}\left(\frac{M_{11}}{A_{1122}}\right)^{1/4}, \tag{10c}$$

and at high frequencies (when the evanescent shear waves start propagating after a cut-off frequency),

$$k_{5,6} \approx \pm\omega_n\sqrt{\frac{M_{11}}{K_1 A_{6611}}}, \quad k_{7,8} \approx \pm\omega_n\sqrt{\frac{K_2 M_{22}}{A_{1122}}}. \tag{10d}$$

There would be a pair of propagating transverse flexural waves and a pair of evanescent shear waves with wavenumbers at low frequencies, respectively,

$$k_{9,10} \approx \pm\sqrt{\omega_n}\left(\frac{M_{11}}{A_{1133}}\right)^{1/4}, \quad k_{11,12} \approx \pm\mathrm{i}\sqrt{\omega_n}\left(\frac{M_{11}}{A_{1133}}\right)^{1/4}, \tag{10e}$$

and at high frequencies (when the evanescent shear waves start propagating after a cut-off frequency),

$$k_{9,10} \approx \pm\omega_n\sqrt{\frac{M_{11}}{K_1 A_{5511}}}, \quad k_{11,12} \approx \pm\omega_n\sqrt{\frac{K_2 M_{33}}{A_{1133}}}. \tag{10f}$$

Here, $K_1$ is the shear correction factor and $K_2$ is the inertia correction factor, which are the adjustable parameters to match the behaviour of the Lamb wave modes in a thick and wide beam cross-section at high frequencies. In context of Timoshenko beam theory, the above correction factors have been discussed by various authors (e.g. Cowper, 1968). In the context of high frequency wave propagation in beams and plates, these correction factors have been evaluated in Doyle (1997). Since, the symmetric thickness or width stretching modes are not included in the first order shear deformable composite beam model, as considered in the present study, the applications of such model should be limited to the frequency range within the first cut-off frequency ($\approx 2\pi c_s/h$) of the symmetric Lamb wave mode pair, where $h$ is the beam depth (or width) and $c_s$ is the phase speed of transverse (or lateral) shear shear wave in the cross-sectional plane $YZ$. Similar frequency range for actual excitation signal and measured signal need to be accounted while comparing and post-processing the data with the simulations based on the above beam waveguide model.

However, for a fully coupled wave propagation in composite, correlating a particular characteristic root (wavenumber) to its mode of propagation is not straight-forward, especially at frequency bands where phase-dispersion cross-over between different modes occur. In this work, we propose a sub-space averaging scheme to speed-up computation. This involves computation of the wavenumbers as in the partially decoupled problems or in other words, the wavenumbers associated with the axial–flexural (method reported in Mahapatra et al. (2000)), axial-torsion and torsion-bending cases. They essentially represent the submatrices in the fully coupled characteristic system $\mathbf{F}(k_j)$ in Eq. (9). Trial roots are then obtained by averaging the computed wavenumbers contributing in the appropriate modes. It is observed that the total number of iterations in the root finding scheme reduces significantly even for strongly coupled configuration arising from asymmetric ply stacking configuration.

As seen in the plot of wavenumber dispersions in Fig. 2, the AS/3501-6 graphite-epoxy unidirectional orthotropic ply stacking configuration with material properties $E_1 = 144.84$ GPa, $E_2 = E_3 = 9.65$ GPa, $G_{13} = G_{12} = 4.14$ GPa, $G_{23} = 3.45$ GPa, $\nu_{12} = \nu_{13} = 0.3$, $\nu_{23} = 0.49$, $\rho = 1389.79$ kg/m$^3$ produces two new propagating shear modes after cut-off frequencies near 60 kHz (for transverse shear, $\theta_y$ mode) and 95 kHz (for lateral shear, $\theta_z$ mode). It also shows that the torsional wave ($\theta_x$ mode) is likely to propagate with the speed, which has same order of magnitude as in transverse flexural wave ($w^0$ mode) and lateral flexural waves ($v^0$ mode). The phase speed ($c_p$) and group speed ($c_g$) are related to the wavenumber ($k_j$) as $c_p = \omega_n/k_j$ and $c_g = \mathrm{d}\omega_n/\mathrm{d}k_j$, respectively. However, deviation from this behaviour is visible in Fig. 3, where the same graphite-epoxy composite is used for $[0°]_8/[90°]_8$ ply stacking. In this case, the transverse flexural wave propagates faster at increasing frequencies compared to the lateral flexural wave. The propagating transverse shear wave appears at a higher cut-off frequency (80 kHz) compared to the corresponding cut-off in the unidirectional case (Fig. 2). The longitudinal wave ($u^0$ mode) propagates dispersively, although the amount of this frequency dependence is low even in presence of maximum possible coupling due to unsymmetric ply orientation ([0°]/[90°] in group).

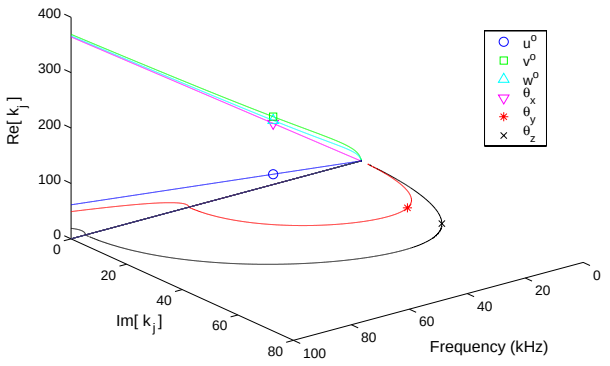


Fig. 2. Wavenumbers for graphite-epoxy unidirectional (0°) ply stacking configuration.

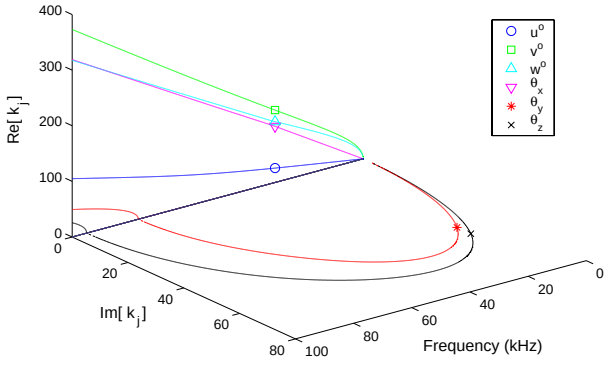


Fig. 3. Wavenumbers for graphite-epoxy asymmetric ($[0]_8/[90°]_8$) ply stacking configuration.

Although the basic steps behind the implementation of SFEM derived here for 3D composite beams with general ply stacking sequence is similar to that in the earlier work (Mahapatra et al., 2000; Mahapatra and Gopalakrishnan, 2003), reducing the complexities while computing the wavenumbers becomes important since overall cost-effectiveness of computation could decrease dramatically when one moves from 2D to 3D analysis with anisotropic material configuration. A general purpose spectral finite element code has been developed for this purpose, which includes several modules intended for a diverse range of applications such as high frequency dynamics of flexible structures, optimization of closed-loop structure-control interaction in wave control applications, modeling of distributed sensors and actuators, impact induced wave propagation in composite etc. It employs sequential root finding scheme with several parametric constraints to compute wavenumbers at each discrete frequencies over user-specified range. To speed-up computation further, a sub-space averaging scheme is proposed to construct the initial guess of the wavenumbers as discussed earlier. This is the most important module, since accuracy of the overall solution depends on how accurately the wavenumbers are computed, especially for full anisotropy in the element constitutive model. After computing the wavenumber at each FFT sampling frequency $\omega_n$ (typically over $2^9$–$2^{15}$ sampling points), the associated matrix of amplitude ratios **R** in Eq. (7) is computed. The numerical steps, and subsequent derivation of the SFEM is given below.

## 3. Spectral finite element model (SFEM)

In order to express all the coupled wave coefficients $\tilde{u}_j$ in Eq. (7) in terms of only 12 primary unknown coefficients associated with 12 primary wave modes, an amplitude ratio matrix $\mathbf{R}_{(6\times12)}$ is introduced. Here, $R_{mj}\tilde{u}_j$ represents the actual wave coefficients in the $m$th displacement components ($m = 1,\ldots,6$) and corresponding to $j$th mode of wave ($j = 1,\ldots,12$). The vector $\mathbf{R}_j$, which forms the $j$th column of the matrix $\mathbf{R}$, is obtained by satisfying the equations

$$\mathbf{F}(k_j)\mathbf{R}_j = \mathbf{0}, \tag{11a}$$

$$R_{mj} = 1 \quad \forall\ \{2(m-1)+1 = j \text{ or } 2(m-1)+2 = j\}, \tag{11b}$$

where, $m$ is one of the displacement component under consideration (e.g. in axial displacement $u^0$, and for propagating longitudinal wave mode pair, $m = 1$ and $j = 1$, 2). After some algebraic manipulations, Eqs. (11a) and (11b) lead to a system of linear equations

$$\begin{bmatrix} F^j_{11} & \cdots & F^j_{1(m-1)} & F^j_{1(m+1)} & \cdots & F^j_{16} \\ \vdots & \ddots & \vdots & \vdots & \ddots & \vdots \\ F^j_{(m-1)1} & \cdots & F^j_{(m-1)(m-1)} & F^j_{(m-1)(m+1)} & \cdots & F^j_{(m-1)6} \\ F^j_{(m+1)1} & \cdots & F^j_{(m+1)(m-1)} & F^j_{(m+1)(m+1)} & \cdots & F^j_{(m+1)6} \\ \vdots & \ddots & \vdots & \vdots & \ddots & \vdots \\ F^j_{61} & \cdots & F^j_{6(m-1)} & F^j_{6(m+1)} & \cdots & F^j_{66} \end{bmatrix} \begin{Bmatrix} R_{1j} \\ \vdots \\ R_{(m-1)j} \\ R_{(m+1)j} \\ \vdots \\ R_{6j} \end{Bmatrix} = -\begin{Bmatrix} F^j_{1m} & \cdots & F^j_{(m-1)m} & F^j_{(m+1)m} & \cdots & F^j_{6m} \end{Bmatrix}^{\mathrm{T}}, \tag{12}$$

where $\mathbf{F}^j = \mathbf{F}(k_j)$. Relative scale of numeric values among different $R_{mj}$ ($\leqslant 1$) represents whether a particular wave mode is strong or weak. Also, they capture the coupling between different displacement components. It is interesting to note that, for 0° ply stacking configuration, we get all $R_{mj} = 0$ except those which satisfy Eq. (11b).

The next step is to eliminate the 12 unknown wave coefficients in $\tilde{\mathbf{u}}$ using six displacement boundary and six force boundary equations (Eqs. (4a)–(4f)). By evaluating Eq. (7) at the element nodes at $x = 0$ and $x = L$ (see Fig. 1), the element nodal displacement vector can be obtained as

$$\hat{\mathbf{u}}^{\mathrm{e}} = \begin{bmatrix} \mathbf{T}_1(0,\omega_n) \\ \mathbf{T}_1(L,\omega_n) \end{bmatrix} \tilde{\mathbf{u}} = \mathbf{T}_2\tilde{\mathbf{u}}. \tag{13}$$

The superscript e to the vector and matrices indicates the spectral element nodal quantities. In Eq. (13), the non-singular (12×12) complex matrix $\mathbf{T}_2$ represents the local wave characteristics of displacement field. Combining Eqs. (7) and (13), an exact shape function matrix $\aleph^{\mathrm{e}}$ for the two node spectral finite element for 3D anisotropic composite beam waveguide (Fig. 1) can be obtained as

$$\hat{\mathbf{u}}(x,\omega_n) = \mathbf{T}_1(x,\omega_n)\mathbf{T}_2^{-1}\hat{\mathbf{u}}^{\mathrm{e}} = \aleph(x,\omega_n)^{\mathrm{e}}\hat{\mathbf{u}}^{\mathrm{e}}. \tag{14}$$

Next, the relationship between the generic displacement vector $\hat{\mathbf{u}}(x,\omega_n)$ and the wave coefficient vector $\tilde{\mathbf{u}}$ in Eq. (7) are used to derive the generic force vector $\hat{\mathbf{f}}(x,\omega_n)$ from the force boundary conditions (Eqs. (4a)–(4f)). This is given by

$$\hat{\mathbf{f}}(x,\omega_n) = \mathbf{Q}_0\mathbf{R}\mathbf{\Lambda}_0\tilde{\mathbf{u}} + \mathbf{Q}_1\mathbf{R}\mathbf{\Lambda}_1\tilde{\mathbf{u}}, \tag{15}$$

where

$$\mathbf{Q}_0 = \begin{bmatrix} 0 & 0 & 0 & 0 & A_{1511} & A_{1611} \\ 0 & 0 & 0 & 0 & A_{5611} & A_{6611} \\ 0 & 0 & 0 & 0 & A_{5511} & A_{5611} \\ 0 & 0 & 0 & 0 & (A_{5521} - A_{5631}) & (A_{5621} - A_{6631}) \\ 0 & 0 & 0 & 0 & A_{1531} & A_{1631} \\ 0 & 0 & 0 & 0 & A_{1521} & A_{1621} \end{bmatrix}, \tag{16}$$

$$\mathbf{Q}_1 = \begin{bmatrix} A_{1111} & A_{1611} & A_{1511} & (A_{1512} - A_{1613}) & A_{1113} & A_{1112} \\ & A_{6611} & A_{5611} & (A_{5612} - A_{6613}) & A_{1613} & A_{1612} \\ & & A_{5511} & (A_{5512} - A_{5613}) & A_{1513} & A_{1512} \\ & \text{Sym.} & & \begin{pmatrix} A_{5522} - 2A_{5623} \\ +A_{6633} \end{pmatrix} & \begin{pmatrix} A_{1523} \\ -A_{1633} \end{pmatrix} & \begin{pmatrix} A_{1522} \\ -A_{1632} \end{pmatrix} \\ & & & & A_{1133} & A_{1123} \\ & & & & & A_{1122} \end{bmatrix} \tag{17}$$

are both (6×6) real matrices as functions of material and cross-sectional properties. $\mathbf{\Lambda}_1$ is a (12×12) diagonal matrix given by

$$\Lambda_1 jj = \frac{\partial}{\partial x}\lambda_0 jj, \quad j = 1, \ldots, 12. \tag{18}$$

By evaluating Eq. (18) at the element boundaries $x = 0, L$ and and substituting $\tilde{\mathbf{u}}$ using Eq. (13), the element nodal force vector can be related to the element nodal displacement vector as

$$\hat{\mathbf{f}}^{\mathrm{e}} = \begin{bmatrix} -(\mathbf{Q}_0\mathbf{R}\mathbf{\Lambda}_0 + \mathbf{Q}_1\mathbf{R}\mathbf{\Lambda}_1)_{x=0} \\ (\mathbf{Q}_0\mathbf{R}\mathbf{\Lambda}_0 + \mathbf{Q}_1\mathbf{R}\mathbf{\Lambda}_1)_{x=L} \end{bmatrix} \mathbf{T}_2^{-1}\hat{\mathbf{u}}^{\mathrm{e}} = \hat{\mathbf{K}}^{\mathrm{e}}\hat{\mathbf{u}}^{\mathrm{e}}. \tag{19}$$

Here, $\widehat{\mathbf{K}}^{\mathrm{e}}$ is a (12×12) complex exact dynamic stiffness matrix for the two node spectral finite element. Transformation of the nodal displacement vector and the nodal force vector from element local coordinate system to global coordinate system can be expressed as

$$\hat{\mathbf{u}}^{\mathrm{g}} = \mathbf{T}\hat{\mathbf{u}}^{\mathrm{e}}, \quad \hat{\mathbf{f}}^{\mathrm{g}} = \mathbf{T}\hat{\mathbf{f}}^{\mathrm{e}}, \tag{20}$$

where the transformation matrix is given by

$$\mathbf{T} = \begin{bmatrix} \mathbf{R} & \mathbf{0} & \mathbf{0} & \mathbf{0} \\ \mathbf{0} & \mathbf{R} & \mathbf{0} & \mathbf{0} \\ \mathbf{0} & \mathbf{0} & \mathbf{R} & \mathbf{0} \\ \mathbf{0} & \mathbf{0} & \mathbf{0} & \mathbf{R} \end{bmatrix}, \tag{21a}$$

$$\mathbf{R} = \begin{bmatrix} l_x & m_x & n_x \\ \dfrac{-m_x\cos\phi - l_x n_x \sin\phi}{\sqrt{1-n_x^2}} & \dfrac{l_x\cos\phi - m_x n_x\sin\phi}{\sqrt{1-n_x^2}} & \sqrt{1-n_x^2}\sin\phi \\ \dfrac{m_x\sin\phi - l_x n_x\cos\phi}{\sqrt{1-n_x^2}} & \dfrac{-l_x\sin\phi - m_x n_x\cos\phi}{\sqrt{1-n_x^2}} & \sqrt{1-n_x^2}\cos\phi \end{bmatrix}, \tag{21b}$$

$l_x$, $m_x$ and $n_x$ are the direction cosines that the beam local $X$-axis makes with the global $(X, Y, Z)$ axis system, $\phi$ is the angle of rotation about the beam local $X$-axis. Finite element assembly is carried out using the global contribution of individual element stiffness matrix of the form

$$\widehat{\mathbf{K}}^{\mathrm{g}} = \mathbf{T}^{\mathrm{T}}\widehat{\mathbf{K}}^{\mathrm{e}}\mathbf{T}. \tag{22}$$

Now, Eq. (22) is to be solved at each FFT sampling frequency $\omega_n$, where the input external nodal excitation is given by

$$\mathbf{f}(t) = \sum_{n=1}^{N} \hat{\mathbf{f}} \mathrm{e}^{\mathrm{i}\omega_n t}. \tag{23}$$

Apart from this major difference compared to time integration or mode superposition in conventional FEM, the SFEM becomes very efficient in terms of system size. This is evident from the above derivation that the exact solution to the wave equation inherited in Eq. (19) allows one to consider a single element over uniform spatial domain. However, additional complexities in wavenumber computation and inversion of $\mathbf{T}_2$ are performed using matrix domain decomposition techniques to speed-up computation. The presented SFEM enables one to use the wave propagation analysis in finite composite beams and plate strips with different types of boundaries with constraints.

### 3.1. Treatment of passive boundary constraints

Passive boundary constraints can be imposed in Eq. (19) using the forms

$$\hat{f}_m^{\mathrm{e}} = -K_m \hat{u}_m^{\mathrm{e}}, \quad \hat{f}_m^{\mathrm{e}} = -\mathrm{i}\omega_n C_m \hat{u}_m^{\mathrm{e}}, \quad \hat{f}_m^{\mathrm{e}} = \omega_n^2 M_m \hat{u}_m^{\mathrm{e}} \tag{24}$$

to model the effects of scattering from elastic joints with spring stiffness $K_m$, scattering from viscous absorber with damping coefficient $C_m$, and scattering from lumped mass $M_m$, respectively. Such treatment in spectral finite element and its applications in isotropic rods and beams can be found in Doyle (1997) and Lee and Kim (2000).

### 3.2. Treatment of active boundary constraints

Active boundary constraints with the help of externally mounted conventional transducers as well as smart embedded actuators and MEMS devices have received renewed interest due to recent developments in smart structural technologies (Bent et al., 1995; Clark et al., 1998; Tupper, 2000). In this context, the wave control applications (Brennan et al., 1997; Castro and Zuazua, 1998; Tanaka and Kikushima, 1999; Mahapatra et al., 2001a) are those in which many practical and engineering issues are yet to be resolved. The present SFEM is one of the suitable model, where various configurations of active boundary control of waves can be studied. Especially, when it comes to the design of acoustic devices for wave control or diagnostic wave generation in damage detection, one or multiple primary wave modes are to be controlled. Here, one can use Eq. (19) along with the active boundary constraint equation of the form

$$\hat{\mathbf{f}}^{\mathrm{e}} = \mathbf{a}(\overline{C}_{jl}, e_{jl}, \epsilon_{kk}, A, \beta)\widehat{E} \tag{25a}$$

for open-loop control, where $\mathbf{a}$ is a vector of nodal cross-sectional property of active material system (e.g. piezoceramic patch actuator) as functions of stiffness $\overline{C}_{jl}$, electro-mechanical coupling coefficients $e_{jl}$ and dielectric constants $\epsilon_{kk}$, actuator sensitivity $\beta$, and cross-sectional area $A$. $\widehat{E}$ is the frequency dependent AC electric field. Similar form can also be employed for magnetostrictive and electro-rheological material system. For closed-loop control, one can use Eq. (19) along with active boundary constraint equation of the form

$$\hat{\mathbf{f}}^{\mathrm{e}} = \mathbf{a}(\overline{C}_{jl}, e_{jl}, \epsilon_{kk}, A, \beta, \gamma)\aleph(x_{\mathrm{s}}, \omega_n)_m \hat{\mathbf{u}}^{\mathrm{e}}, \tag{25b}$$

where $\gamma$ is the feedback gain, $\aleph(x_{\mathrm{s}}, \omega_n)_m$ is the vector comprising of $m$th row of the shape function matrix as a function of the error sensor location $x_{\mathrm{s}}$ within the element. A detail derivation of a generalized form of feedback control of waves can be found (Mahapatra et al., 2001a). There are certain practical significance

behind considering such passive or active boundary control forces in the present context of finite element modeling. One of the major significance is that in laminated composite, the surface bonded or embedded transducers for structural control and structural health monitoring may develop progressive debonding or delaminations. Therefore, in the process of detecting such debonding or delaminations, it is essential to consider the on-line influence of these transducers, and Eqs. (24) and (25) serve well that purpose.

### 3.3. Treatment of waves in bounded media

Although, the present derivation in SFEM deals with beam waveguide with the boundary nodes along the beam axis, a fair representation of beams immersed in viscoelastic solid can be given within this framework. The basic idea on which this treatment is carried out, can be traced back to the works of Seeling and Hoppmann (1964) and Doyle (1997) on wave propagation in double beam structure coupled by distributed spring. The following treatment of beam waveguide in bounded media has practical applications while treating wave transmission and scattering due to inclusions having beam type structures (embedded MEMS devices or elctronic chips inside composite). Also, such model can be used for modeling friction contact between the delaminated surfaces in laminated composite (Luo and Hanagud, 2000). Here, one can consider the beam waveguide of interest (denoted as $p$) placed within two surrounding waveguides (also considered as beam waveguides here, and are denoted by $p-1$ and $p+1$ respectively) as shown in Fig. 4. The interface at the top and bottom surfaces of the waveguide $p$ are viscoelastic Maxwell solid of finite thickness modeled with distributed spring constants $K_x$, $K_y$ and $K_z$, and distributed viscous damping coefficients $C_x$, $C_y$ and $C_z$, corresponding to displacements $u$, $v$ and $w$. Now, let us consider the spectral amplitude of the distributed load vectors (consisting of three forces in $x$, $y$, $z$ and three moments about $x$, $y$, $z$) $\widehat{\mathbf{\Gamma}}_{(p)\mathrm{t}}$ for the top surface ($XY$ plane at $z = z_{(p,p+1)}$) and $\widehat{\mathbf{\Gamma}}_{(p)\mathrm{b}}$ for the bottom surface ($XY$ plane at $z = z_{(p,p-1)}$) of the waveguide $p$. One can write

$$\begin{aligned}\widehat{\mathbf{\Gamma}}_{(p)\mathrm{t}} &= \begin{bmatrix} K_x + \mathrm{i}\omega_n C_x & 0 & 0 \\ 0 & K_y + \mathrm{i}\omega_n C_y & 0 \\ 0 & 0 & K_z + \mathrm{i}\omega_n C_z \\ 0 & 0 & 0 \\ z_{\mathrm{t}}(K_x + \mathrm{i}\omega_n C_x) & 0 & 0 \\ 0 & 0 & 0 \end{bmatrix} \begin{Bmatrix} \hat{u}_{(p+1)\mathrm{b}} - \hat{u}_{(p)\mathrm{t}} \\ \hat{v}_{(p+1)\mathrm{b}} - \hat{v}_{(p)\mathrm{t}} \\ \hat{w}_{(p+1)\mathrm{b}} - \hat{w}_{(p)\mathrm{t}} \end{Bmatrix} \\ &= \mathbf{K}^*_{(p,p+1)}(\hat{\mathbf{u}}_{(p+1)\mathrm{b}} - \hat{\mathbf{u}}_{(p)\mathrm{t}}), \end{aligned} \tag{26}$$

where the subscripts t and b respectively indicate the top surface and the bottom surface of a waveguide (indicated by subscript with bracket). With the help of Eqs. (1a)–(1c),

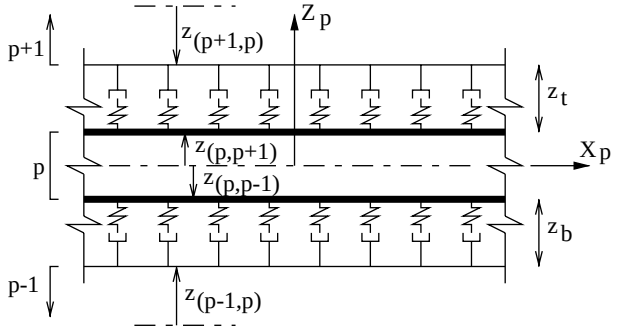


Fig. 4. Schematic diagram showing the beam waveguide $p$ in bounded viscoelastic media.

$$\begin{Bmatrix} \hat{u}_{(p)\mathrm{t}} \\ \hat{v}_{(p)\mathrm{t}} \\ \hat{w}_{(p)\mathrm{t}} \end{Bmatrix} = \begin{bmatrix} 1 & 0 & 0 & 0 & z_{(p,p+1)} & y_{(p,p+1)} \\ 0 & 1 & 0 - z_{(p,p+1)} & 0 & 0 & \\ 0 & 0 & 1 & y_{(p,p+1)} & 0 & 0 \end{bmatrix} \hat{\mathbf{u}}(x,\omega_n)_{(p)} = \mathbf{S}_{(p,p+1)} \aleph^{\mathrm{e}}_{(p)} \hat{\mathbf{u}}^{\mathrm{e}}_{(p)}. \tag{27}$$

Similar expression holds for the bottom surface of the waveguide $p$. Finally, the resultant consistent element nodal load vector is obtained in terms of the distributed load vectors and the exact shape function matrices for the waveguides, which can be written as

$$\hat{\mathbf{f}}^{\mathrm{e}} = \int_0^L \aleph^{\mathrm{e}^{\mathrm{T}}}_{(p)} (\widehat{\mathbf{\Gamma}}_{(p)\mathrm{t}} + \widehat{\mathbf{\Gamma}}_{(p)\mathrm{b}})\, \mathrm{d}x, \tag{28a}$$

$$\begin{aligned} \Rightarrow \hat{\mathbf{f}}^{\mathrm{e}} = & \left[ \int_0^L \aleph^{\mathrm{e}^{\mathrm{T}}}_{(p)} \mathbf{K}^{*}_{(p,p+1)} \mathbf{S}_{(p+1,p)} \aleph^{\mathrm{e}}_{(p+1)}\, \mathrm{d}x \right] \hat{\mathbf{u}}^{\mathrm{e}}_{(p+1)} - \left[ \int_0^L \aleph^{\mathrm{e}^{\mathrm{T}}}_{(p)} \mathbf{K}^{*}_{(p,p+1)} \mathbf{S}_{(p,p+1)} \aleph^{\mathrm{e}}_{(p)}\, \mathrm{d}x \right] \hat{\mathbf{u}}^{\mathrm{e}}_{(p)} \\ & - \left[ \int_0^L \aleph^{\mathrm{e}^{\mathrm{T}}}_{(p)} \mathbf{K}^{*}_{(p,p-1)} \mathbf{S}_{(p,p-1)} \aleph^{\mathrm{e}}_{(p)}\, \mathrm{d}x \right] \hat{\mathbf{u}}^{\mathrm{e}}_{(p)} + \left[ \int_0^L \aleph^{\mathrm{e}^{\mathrm{T}}}_{(p)} \mathbf{K}^{*}_{(p,p-1)} \mathbf{S}_{(p-1,p)} \aleph^{\mathrm{e}}_{(p-1)}\, \mathrm{d}x \right] \hat{\mathbf{u}}^{\mathrm{e}}_{(p-1)}. \end{aligned} \tag{28b}$$

### 3.4. Treatment of perfectly absorbing boundary: throw-off spectral element

In many numerical simulations of wave propagation in finite domain, it is useful to eliminate the boundary reflections. Also, in the solution methods in transformed domain (such as the present SFEM, which is formulated in Fourier domain and numerical treatment is done using FFT), distortion of the temporal response appears as a result of insufficient length of the time window, when the system in undamped and hence the response does not decay at the end of the window. Such an inherent problem during forward and inverse FFT is handled in SFEM by introducing a small amount of damping $\eta$ through wavenumber as $k_j \leftarrow k_j(1 - \mathrm{i}\eta)$. However, in situations, where a very high amount of energy gets trapped within a finite waveguide and one still needs to study certain local phenomena, where the farfield reflections are unwanted, we can assume $L \to \infty$. This leads to the vanishing backward propagating and backward evanescent wave modes (columns $j = 2, 4, 6, 8, 10$ and 12 in the amplitude ratio matrix $\mathbf{R}$. By removing the corresponding wave coefficients $\tilde{u}_j$ in $\tilde{\mathbf{u}}$ and condensing out $\mathbf{R}$ to a $6\times6$ matrix in Eq. (7) and subsequent derivations, we obtain a single node throw-off spectral element.

## 4. A sub-laminate-wise constant shear kinematics model for multiple delaminations and strip inclusions

While modeling the delaminations in composite structures, spatial discretization becomes difficult while using standard finite elements. Available finite element packages generally use plate-bending element or degenerated shell elements, which cannot be used in the interfacial regions where more than one sub-laminates form the base-laminate. Moreover, due to significant difference in the order of thickness and planer dimensions, planer or solid elements, when used at the interfaces, yield enormous system size. In addition, there is always high computational cost to handle such a large system size to capture highly transient pulse propagation. Use of such high frequency modulated pulse has been found efficient as in wave based diagnostics in smart structural health monitoring (Park et al., 2000; Lin and Yuan, 2001; Nag et al., 2002). In the present study, a systematic derivation is presented to model the interfaces between the base-laminate and multiple sub-laminates in a general form. When one of the intermediate sub-laminates are of different material configuration, it can be treated as strip inclusion. The idea is to capture the wave transmission and scattering at these delamination tips or at the interfaces between the inclusions and the

host materials using diagnostic signal. The SFEM discussed in the previous section is used as basic building block for the spectral interface model.

As it has been discussed in the introduction that there are difficulties in available methods for modeling delaminations and inclusions, which needs further development. In this paper, our main objective is to construct and solve a set of constrained equations in Fourier domain (consistent with the framework of SFEM) for multiple delaminations and inclusions by allowing discontinuity in the rotation $\theta_y$ of the cross-sectional plane between two sub-laminates above and below delaminations. The delaminated configuration is shown in Fig. 5. This also allows a particular sub-laminate made of different materials to be treated as strip inclusion debonded from the host materials. For simplicity, we assume that the dynamics of the delaminations or slip between the inclusion and host materials is governed by Mode-II fracture process, excluding any effect of Mode-I fracture (opening and closing of delaminations causing interpenetration and incompatibility in $z$ direction, Luo and Hanagud, 2000).

The formulation is generalized by considering two cases as shown in Fig. 6. In case (a) (Fig. 6(a)), two consecutive nodes $p$ and $q$ are considered on the interface, which connect two elements on opposite sides of the interface. Since, there is no delamination between node $p$ and node $q$, in-plane displacements and rotation of normal planes at these nodes can be constrained as

$$u_p^0 + z_{pq}\theta_y p = u_q^0, \quad \theta_y p = \theta_y q, \tag{29a}$$

where $z_{pq}$ is the distance along $z$ direction between the node $p$ and node $q$. In case (b) (Fig. 6(b)), a single delamination is considered between node $p$ and node $q$, which are on the same face on the interface. Each

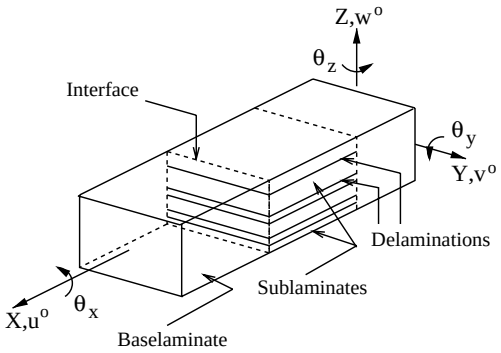


Fig. 5. Schematic diagram showing multiple through-width delaminations in a laminated composite beam.

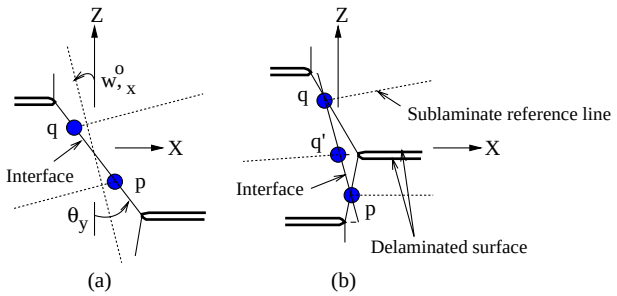


Fig. 6. Interfacial nodes taking part in constrained kinematics of base-laminate and sub-laminates or debonded strip inclusions.

of these nodes belongs to the element representing one of the sub-laminate above or below the delamination. Node $q'$ on the other side of the interface belongs to the element representing base-laminate. Since, under the assumption of sub-laminate-wise constant shear, the normal plane passing through node $q'$ has to rotate in a rigid body mode, the discontinuous plane passing through node $p$ and node $q$ must rotate in a constrained manner. Such constraint can be imposed as follows. Interface in the region including node $p$ and node $q'$ is already defined in Eq. (29a) representing the case (a). Now, one needs to construct the constrained equations for interfacing the node $p$ and node $q$. This can be expressed as

$$u_p^0 + z_{pt}\theta_y p = u_q^0 + z_q \mathrm{b}\theta_y q, \tag{29b}$$

where $z_{pt}$ is the depth of the top surface of the sub-laminate containing node $p$ and measured from the corresponding element local reference line. Similarly, $z_{q\mathrm{b}}$ is the depth of the bottom surface of the sub-laminate containing node $q$ and measured from the corresponding element local reference line. For all other nodal displacement components associated with the node $p$ and node $q$, the equations for constraint can be written as

$$v_p^0 = v_q^0, \quad w_p^0 = w_q^0, \quad \theta_x p = \theta_x q, \quad \theta_z p = \theta_z q. \tag{29c}$$

Implementation of the above displacement constraints can be automated to model multiple delaminations or inclusions across the thickness as well as for different variances of such configuration at various locations along the length of a beam. Eqs. (29a)–(29c) can be assembled at the global level with appropriate transformation to form the multi-point constraint (MPC) equation in nodal displacement vector. Let us consider Eq. (29a) obtained in case (a) along with Eq. (29c). We can write these six equations in matrix form as

$$\begin{bmatrix} 1 & 0 & 0 & 0 & z_{pq} & 0 & -1 & 0 & 0 & 0 & 0 & 0 \\ 0 & 1 & 0 & 0 & 0 & 0 & 0 & -1 & 0 & 0 & 0 & 0 \\ 0 & 0 & 1 & 0 & 0 & 0 & 0 & 0 & -1 & 0 & 0 & 0 \\ 0 & 0 & 0 & 1 & 0 & 0 & 0 & 0 & 0 & -1 & 0 & 0 \\ 0 & 0 & 0 & 0 & 1 & 0 & 0 & 0 & 0 & 0 & -1 & 0 \\ 0 & 0 & 0 & 0 & 0 & 1 & 0 & 0 & 0 & 0 & 0 & -1 \end{bmatrix} \begin{Bmatrix} \hat{u}_p^0 \\ \vdots \\ \hat{\theta}_{zp} \\ \hat{u}_q^0 \\ \vdots \\ \hat{\theta}_{zq} \end{Bmatrix} = \mathbf{0}. \tag{30a}$$

Now, for example, if the node numbering is $p$, $p+1$ and $q$, $q+1$ for the two elements connected to the interface, then Eq. (30a) can be rewritten as

$$[\mathbf{C}_{\mathbf{u}1} \quad \mathbf{0} \quad | \quad \mathbf{C}_{\mathbf{u}2} \quad \mathbf{0}] \begin{Bmatrix} \mathbf{T}^{\mathrm{T}} \hat{\mathbf{u}}_p^{\mathrm{g}} \\ \mathbf{T}^{\mathrm{T}} \hat{\mathbf{u}}_q^{\mathrm{g}} \end{Bmatrix} = \mathbf{0}, \tag{30b}$$

where $\mathbf{C}_{\mathbf{u}1}$ and $\mathbf{C}_{\mathbf{u}2}$ are the two $6\times6$ sub-matrices in Eq. (30a). Similar form is also obtained for interface in case (b). Finally, all these equations of displacement constraints can be assembled to form a single matrix equation at the global level, which is given by

$$\mathbf{C}_{\mathbf{u}} \hat{\mathbf{u}}^{\mathrm{g}} = \mathbf{0}. \tag{30c}$$

Next, the equilibrium of the nodal forces at each interface is to be established. This is obtained as

$$\sum_p \mathbf{S}_p'^{\mathrm{T}} \hat{\mathbf{f}}_p^{\mathrm{e}} = \hat{\mathbf{f}}, \tag{31a}$$

where the summation sign stands for all the nodes in a particular cross-section. $\hat{\mathbf{f}}$ is the applied load vector at the interface under consideration. For an element with nodes numbered $p$, $p+1$ and the node $p$ on the interface,

$$\mathbf{S}'_p = \left[\begin{array}{cccccc|c} 1 & 0 & 0 & 0 & h_p & 0 & \\ 0 & 1 & 0 & 0 & 0 & 0 & \\ 0 & 0 & 1 & 0 & 0 & 0 & \\ 0 & 0 & 0 & 1 & 0 & 0 & \mathbf{0} \\ 0 & 0 & 0 & 0 & 1 & 0 & \\ 0 & 0 & 0 & 0 & 0 & 1 & \end{array}\right] \tag{31b}$$

$h_p$ is the distance of the node $p$ in $z$ direction measured from the bottom surface of the beam. Eq. (31b) can be rewritten in terms of the element nodal displacement vector at the global level as

$$\sum_p \mathbf{S}'_p \mathbf{T}^{\mathrm{T}} \widehat{\mathbf{K}}^{\mathrm{e}}_p \mathbf{T} \hat{\mathbf{u}}^{\mathrm{g}}_p = \mathbf{T}^{\mathrm{T}} \hat{\mathbf{f}}^{\mathrm{g}}. \tag{31c}$$

Eq. (31c) can be assembled to form a single matrix equation involving force constraints at the global level, which is given by

$$\mathbf{C}_{\mathbf{f}} \hat{\mathbf{u}}^{\mathrm{g}} = \mathbf{f}'. \tag{31d}$$

Now, we use two diagonal matrices of penalty parameters $\boldsymbol{\alpha}_{\mathbf{u}}$ and $\boldsymbol{\alpha}_{\mathbf{f}}$ to impose the displacement constraints in Eq. (30c) and force constraints in Eq. (31d) respectively, to minimize the stationary potential

$$\widehat{\boldsymbol{\Pi}} = \frac{1}{2} \hat{\mathbf{u}}^{\mathrm{g}^{\mathrm{T}}} \widehat{\mathbf{K}}^{\mathrm{g}} \hat{\mathbf{u}}^{\mathrm{g}} - \hat{\mathbf{u}}^{\mathrm{g}^{\mathrm{T}}} \hat{\mathbf{f}}^{\mathrm{g}} + \frac{1}{2} (\mathbf{C}_{\mathbf{u}} \hat{\mathbf{u}}^{\mathrm{g}})^{\mathrm{T}} \boldsymbol{\alpha}_{\mathbf{u}} (\mathbf{C}_{\mathbf{u}} \hat{\mathbf{u}}^{\mathrm{g}}) + \frac{1}{2} (\mathbf{C}_{\mathbf{f}} \hat{\mathbf{u}}^{\mathrm{g}} - \mathbf{f}')^{\mathrm{T}} \boldsymbol{\alpha}_{\mathbf{u}} (\mathbf{C}_{\mathbf{f}} \hat{\mathbf{u}}^{\mathrm{g}} - \mathbf{f}') \tag{32}$$

in frequency domain at each $\omega_n$. Minimizing the above potential with respect to the global displacement vector $\hat{\mathbf{u}}^{\mathrm{g}}$, we get the spectral finite element equilibrium equation as

$$(\widehat{\mathbf{K}}^{\mathrm{g}} + \mathbf{C}^{\mathrm{T}}_{\mathbf{u}} \boldsymbol{\alpha}_{\mathbf{u}} \mathbf{C}_{\mathbf{u}} + \mathbf{C}^{\mathrm{T}}_{\mathbf{f}} \boldsymbol{\alpha}_{\mathbf{f}} \mathbf{C}_{\mathbf{f}}) \hat{\mathbf{u}}^{\mathrm{g}} = \hat{\mathbf{f}}^{\mathrm{g}} + \mathbf{C}^{\mathrm{T}}_{\mathbf{f}} \boldsymbol{\alpha}_{\mathbf{f}} \mathbf{f}'. \tag{33}$$

Note that the constraint equations (Eqs. (30c) and (31d)) involve dissimilar DOFs, whose motion is governed by the stiffness coefficients $\mathbf{A}_{jl}$ and inertial coefficients $\mathbf{M}$, which are of varying order. Therefore, use of penalty parameters $\boldsymbol{\alpha}_{\mathbf{u}}$ and $\boldsymbol{\alpha}_{\mathbf{f}}$ consistent with the associated DOFs to achieve sufficient numerical accuracy (Cook et al., 1989) is important. Note the order of the values in the additional entries in the updated dynamic stiffness matrix in Eq. (33), that is

$$\mathrm{O}(\mathbf{C}^{\mathrm{T}}_{\mathbf{u}} \mathbf{C}_{\mathbf{u}}) \approx (-6, 0), \quad \mathrm{O}(\mathbf{C}^{\mathrm{T}}_{\mathbf{f}} \mathbf{C}_{\mathbf{f}}) \approx \mathrm{O}\left( \min\left( \widehat{k}^{\mathrm{e2}}_{jj} \right), \max\left( \widehat{k}^{\mathrm{e2}}_{jj} \right) \right), \tag{34}$$

because in $\mathbf{C}_{\mathbf{u}}$, the entries are either 1 or $z_{pq}$ (depth of a composite beam sub-laminates are typically in the order of mm). These lead to

$$\boldsymbol{\alpha}_{\mathbf{u}} jj = |\widehat{k}^{\mathrm{e}}_{jj}| \times 10^9, \quad \boldsymbol{\alpha}_{\mathbf{f}} jj = |\widehat{k}^{\mathrm{e}-1}_{jj}| \times 10^3 \tag{35}$$

as a convenient choice of the penalty parameters while solving the constrained system in Eq. (33) at each sampling frequency $\omega_n$, $n = 1, \ldots, N$.

## 5. Spectral power flow: a diagnostic measure of wave scattering due to structural discontinuities

After having a finite element model for multiple delaminations and strip inclusions, we need a frequency domain measure, which can quantify the severity of structural discontinuity from the energy transmission point of view. Here we consider the spectral power (Howard et al., 2000)

$$\widehat{P} = \frac{1}{2}\hat{\mathbf{f}}^{\mathrm{T}}[\mathrm{i}\omega_n\hat{\mathbf{u}}]^* \tag{36}$$

as the product of force vector and complex conjugate of velocity vector at a material point.

*Properties of spectral power*:

(1) Real part of the spectral power is space invariant.

Let us consider the coupled wave propagation involving $u^0$, $w^0$ and $\theta_y$. Lateral motion and torsional motion are excluded to reduce the level of algebraic manipulation. Expanding Eq. (36), we have

$$\widehat{P} = -\frac{1}{2}\mathrm{i}\omega_n[(A_{1111}\hat{u}_{,x} + A_{1113}\hat{\theta}_{y,x})\hat{u}^* + A_{5511}(\hat{w}_{,x} + \phi)\hat{w}^* + (A_{1113}\hat{u}_{,x} + A_{1133}\hat{\theta}_{y,x})\hat{\theta}_y^*]. \tag{37a}$$

Differentiating with respect to $x$ and simplifying using the wave equations in $u^0$, $w^0$ and $\theta_y$, we get

$$\begin{aligned}\frac{\partial\widehat{P}}{\partial x} = -\frac{1}{2}\mathrm{i}\omega_n[&-\omega_n^2 M_{11}(\hat{u}^0\hat{u}^{0*} + \hat{w}^0\hat{w}^{0*}) + A_{1111}\hat{u}^0{}_{,x}\,\hat{u}^{0*}{}_{,x} + A_{5511}\hat{w}^0{}_{,x}\,\hat{w}^{0*}{}_{,x} + (A_{5511} - \omega_n^2 M_{33})\hat{\theta}_y\hat{\theta}_y^* \\ &+ A_{1133}\hat{\theta}_{y,x}\hat{\theta}_{y,x}^* - \omega_n^2 M_{13}(\hat{\theta}_y\hat{u}^{0*} + \hat{u}\hat{\theta}_y^*) + A_{5511}(\hat{\theta}_y\hat{w}^{0*}{}_{,x} + \hat{\theta}_y^*\hat{w}^0{}_{,x}) + A_{1113}(\hat{\theta}_{y,x}\hat{u}^{0*}{}_{,x} + \hat{\theta}_{y,x}^*\hat{u}^0{}_{,x})].\end{aligned} \tag{37b}$$

Note that in Eq. (37b), the right hand side is purely an imaginary quantity. Therefore, by equating the real part and imaginary part of the spectral power $\widehat{P} = \widehat{P}_{\mathrm{R}} + \mathrm{i}\widehat{P}_{\mathrm{I}}$, we get

$$\frac{\partial\widehat{P}_{\mathrm{R}}}{\partial x} = 0. \tag{37c}$$

(2) Real part of the spectral power indicates the amount of energy trapped in a structural member.

Using Eq. (37a), it can be shown that for purely longitudinal wave

$$\hat{u}^0 = \tilde{u}_1\mathrm{e}^{-\mathrm{i}k_1 x} + \tilde{u}_2\mathrm{e}^{-\mathrm{i}k_1(L-x)} \tag{38a}$$

the real part of the spectral power

$$\widehat{P}_{\mathrm{R}} = \frac{1}{2}\omega_n k_1 A_{1111}[-\tilde{u}_1\tilde{u}_1^* + \tilde{u}_2\tilde{u}_2^*] \tag{38b}$$

is a stationary quantity and vanishes when

$$|\tilde{u}_1| = |\tilde{u}_2| \tag{38c}$$

that is when the forward and backward propagating waves are of same amplitude. This necessitates the two longitudinal forces ($\widehat{N}_{x1}$ and $\widehat{N}_{x2}$) at the boundaries either to be equal and opposite in sign and hence self-equilibrating or such that the wave coefficients $\tilde{u}_1$ and $\tilde{u}_2$ are with relative phase $\phi_1 - \phi_2$ given by

$$\mathrm{e}^{\mathrm{i}(\phi_1-\phi_2)} = \frac{\widehat{N}_{x2} - \widehat{N}_{x1}\mathrm{e}^{\mathrm{i}k_1 L}}{\widehat{N}_{x2}\mathrm{e}^{\mathrm{i}k_1 L} - \widehat{N}_{x1}}. \tag{38d}$$

Similar conclusions can be drawn from purely transverse flexural waves

$$\hat{w}^0 = \tilde{u}_9\mathrm{e}^{-\mathrm{i}k_9 x} + \tilde{u}_{10}\mathrm{e}^{-\mathrm{i}k_9(L-x)} + \tilde{u}_{11}\mathrm{e}^{-k_9 x} + \tilde{u}_{12}\mathrm{e}^{-k_9(L-x)}, \tag{38e}$$

$$\hat{\theta}_y = R_{5,9}\tilde{u}_9\mathrm{e}^{-\mathrm{i}k_9 x} + R_{5,10}\tilde{u}_{10}\mathrm{e}^{-\mathrm{i}k_9(L-x)} + R_{5,11}\tilde{u}_{11}\mathrm{e}^{-k_9 x} + R_{5,12}\tilde{u}_{12}\mathrm{e}^{-k_9(L-x)}, \tag{38f}$$

$$\widehat{P}_{\mathrm{R}} = \frac{1}{2}\omega_n k_9[-(A_{5511} + A_{1133}R_{5,9}R^*_{5,9})\tilde{u}_9\tilde{u}^*_9 + (A_{5511} + A_{1133}R_{5,10}R^*_{5,9})\tilde{u}_{10}\tilde{u}^*_{10}]. \tag{38g}$$

From Eq. (38g), it is clear that the real part of the spectral power is stationary and vanishes when

$$|R_{5,9}\tilde{u}_9| = |R_{5,10}\tilde{u}_{10}| \tag{38h}$$

that is when the forward and backward propagating wave components in transverse as well as rotational motions are of same amplitude, since $R_{5,9} = -R_{5,10}$ and $R_{5,11} = -R_{5,12}$. This can happen when the pair of boundary forces (transverse shear forces and moments) are self-equilibrating in nature or they are of same amplitude and generates certain relative phase between the forward and backward propagating wave coefficients similar to that in Eq. (38d). In addition, note that in the real part of the spectral power, there is no contribution of evanescent wave component.

(3) The imaginary part of the spectral power carries the phase information.

Here we illustrate the traveling nature of the power wave. Let us consider the longitudinal wave propagation (Eq. 38a). Using Eq. (36), the imaginary part of the spectral power is obtained as

$$\widehat{P}_{\mathrm{I}} = \tilde{P}_1 \mathrm{e}^{-\mathrm{i}2k_1 x} - \tilde{P}^*_1 \mathrm{e}^{\mathrm{i}2k_1 x}, \tag{39a}$$

where the power wave coefficients $\tilde{P}_1$ and $-\tilde{P}^*_1$ (* indicates complex conjugation) associated with the forward and backward traveling power wave components are given by

$$\tilde{P}_1 = \frac{1}{2}\mathrm{i}\omega_n k_1 A_{1111}\tilde{u}_1\tilde{u}^*_2 \mathrm{e}^{\mathrm{i}k_1 L}. \tag{39b}$$

Therefore, if there is no change in the geometry and material properties between the two boundary nodes, the traveling wave causes flow of power, which has equal amplitudes in the forward and backward propagating power waves as seen in Eq. (39a).

### 5.1. Measure of wave scattering due to delaminations and inclusions using spectral power

From the above discussions, it is quite clear that any structural discontinuity inside a structural member would create scattered waves due to change in the wave coefficients by certain factor called scattering coefficient. This in turn, would cause changes in energy transmission and hence the power flow. To study the effect of delaminations and strip inclusions, we consider two nodal points (1 and 2) along the beam $x$-axis with associated spectral power $\widehat{P}_1$ and $\widehat{P}_2$ on the two sides of delaminations or inclusions. Then we construct a measure of scattered power as

$$\Delta = \sum_{n=n_1}^{n_2} \frac{|\widehat{P}(\omega_n)_{\mathrm{h}} - \widehat{P}(\omega_n)_{\mathrm{d}}|}{|\widehat{P}(\omega_n)_{\mathrm{h}}|}, \tag{40}$$

where $\widehat{P}(\omega_n)_{\mathrm{h}}$ and $\widehat{P}(\omega_n)_{\mathrm{d}}$ are respectively the scattered power $\widehat{P}_1 - \widehat{P}_2$ for healthy structure and the structure with discontinuities. We denote the power measure in Eq. (40) over the frequency band $n = [n_1, n_2]$. In the numerical simulations, we estimate the effect of delaminations and inclusions using three frequency bands: low ($\omega_n = 1$ Hz–1 kHz), medium ($\omega_n = 1$–10 kHz) and high ($\omega_n = 10$–100 kHz).

## 6. Numerical simulations

### 6.1. Transverse, lateral and torsional impact induced wave propagation

In this section we simulate the propagation of transverse, lateral and torsional waves in an angle-joint connecting three composite beam members. Each of these members are assumed as 0° unidirectional graphite-epoxy with 10 mm × 10 mm cross-section. The rigid joint angle is $\phi = 45°$ in $XZ$ plane. Each member is 0.5 m long and lie in the $XZ$ plane. Three semi-infinite throw-off spectral elements are used towards the other end of the members.

#### 6.1.1. Effect of transverse impact

Fig. 7 shows the impact load history used in the analysis. This load is applied at point B in transverse direction ($f_z(t)$ as shown in the inset of Fig. 8). The transverse velocity $\dot{w}$ histories at points B and A are shown in Fig. 8. The figure shows the arrival of transmitted flexural–shear wave at point A at the same time as the arrival of the reflected wave from the joint at point B. This is because the inclined member lies in the $XZ$ plane, which produces only axial–flexural–shear coupled motion and no torsional motion under the loading in $XZ$ plane. This is unlike the lateral flexural case as will be evident next, where the loading is in $XY$ plane and hence produces torsional waves after transmission through the joint.

#### 6.1.2. Effect of lateral impact

Propagation of lateral flexural wave is studied by applying the impact load (Fig. 7) at point B in lateral direction ($f_y(t)$ as shown in the inset of Fig. 9). The lateral velocity $\dot{v}$ histories at points B and A are shown in Fig. 9. The figure shows the arrival of transmitted flexural–shear wave at point A at 0.5 ms which is little earlier than the arrival time of the reflected wave from the joint at point B. This can be attributed to the fact that the lateral impact at point B produced coupled flexural–shear–torsional wave during transmission through the joint due to the inclined member. Since the speed of the torsional wave is slightly higher than the speed of the propagating flexural wave but smaller than the speed of the propagating shear wave, as seen from the figure of wavenumbers $k = \omega/c$ in Figs. 2 and 3, the arrival time of the coupled flexural–shear–torsional wave is earlier at point A than at point B.

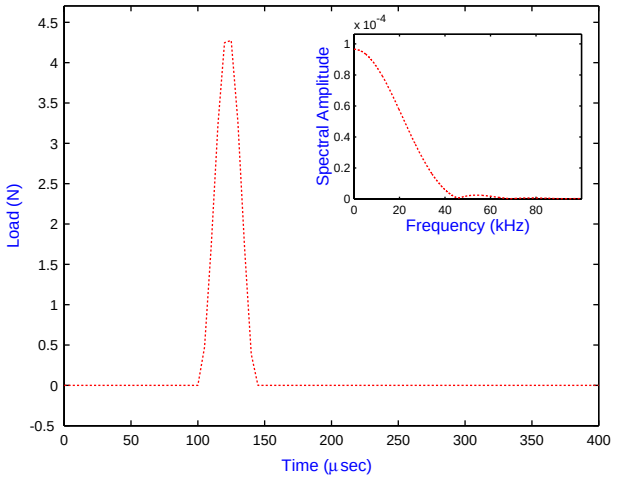


Fig. 7. Time history of a broadband load of 50 μs duration. The frequency spectrum is shown in the inset.

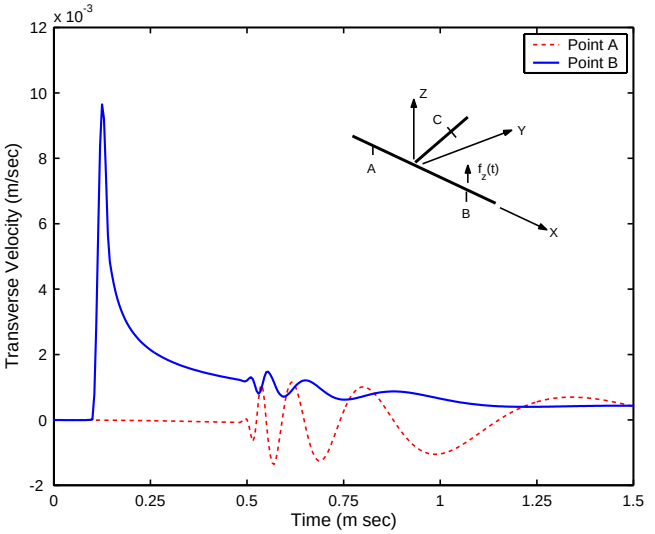


Fig. 8. Transverse velocity ($\dot{w}$) histories at points B and A due to the impact load $f_z(t)$ (Fig. 7) applied at point B.

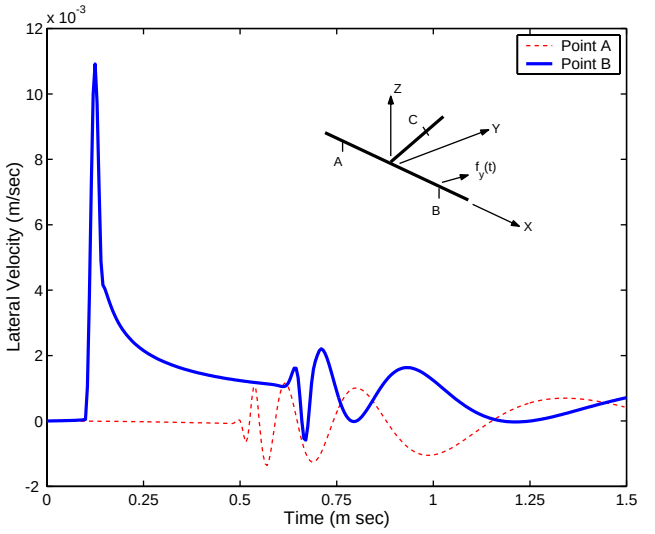


Fig. 9. Lateral velocity ($\dot{v}$) histories at points B and A due to the impact load $f_y(t)$ (Fig. 7) applied at point B.

### 6.1.3. *Effect of torsional impact*

Propagation of torsional wave is studied by applying a similar impact load as considered in the previous cases (amplitudes in N m scale) at point B ($f_\theta(t) = f_{\theta_x}(t)$ and its direction vector as shown in the inset of Fig. 10). The rotational velocity $\dot{\theta}_x$ histories at points B and A are shown in Fig. 10. Since the torsional mode is non-dispersive under the present kinematic assumption for symmetric ply stacking configuration, a sign change in the reflected peak arrived at point B from the joint can be seen. On the other hand the transmitted wave arrived at point A can be seen with the same sign as the incident pulse.

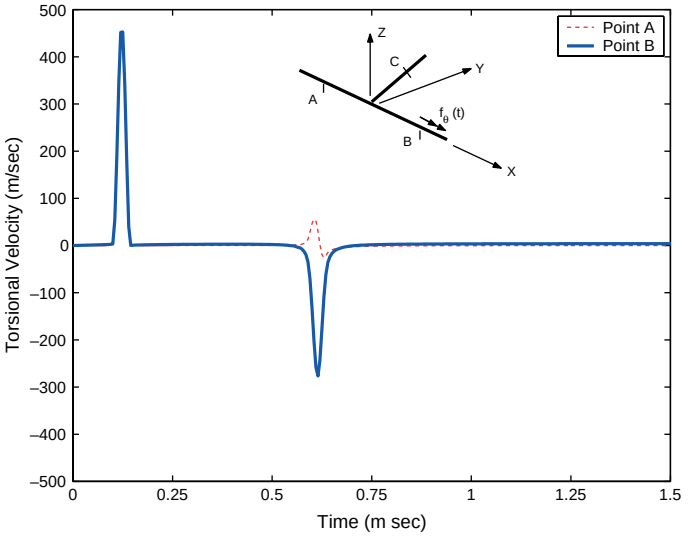


Fig. 10. Rotational velocity ($\dot{\theta}_x$) histories at points B and A due to the impact load $f_\theta(t)$ applied at point B.

### 6.2. Wave scattering from delamination: comparison with 2D FEM

The quality of the results from the SFEM with sub-laminate-wise constant shear kinematics model proposed in this paper are validated by comparing with the results obtained from a 2D plane stress FEM. A unidirectional graphite-epoxy $[0°]_{80}$ composite cantilever beam of length 0.8 m, thickness 16 mm, width 10 mm with a 50 mm mid-plane delamination is considered. The center of delamination is 0.4 m away from the fixed end of the beam. A single frequency sinusoidal pulse modulated at 20 kHz (Fig. 11) is applied transversely at the tip. Use of such high frequency modulated pulse has been found suitable for identification of delamination (Nag et al., 2002). Issues related to instrumentation and signal generation of such

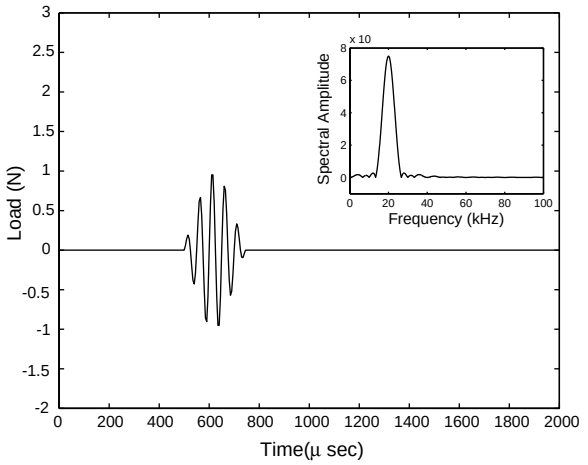


Fig. 11. Single frequency sinusoidal pulse modulated at 20 kHz using trapizoidal window. The spectral amplitude $\hat{f}$ over the frequency axis is shown in inset.

diagnostic wave for integrated smart structural health monitoring systems have been discussed in Valdez and Soutis (2001), Lin and Yuan (2001) and Kessler et al. (2002). In SFEM, four elements (two for base-laminates and two for sub-laminates above and below the delamination) with 4096 FFT sampling points ($\Delta\omega = 48.828$ Hz) are used. In 2D plane stress FEM in $XZ$ plane, a fine mesh consisting of 2560 constant strain triangular elements and Newmark's time integration is used. Here, the element size is comparable with the wavelength of applied excitation. Fig. 12 shows the comparison of transverse velocity history $\dot{w}$ at the free end mid-plane. The first pulse starting at 0.5 ms is due to the incident load at the tip. After this, only the first reflection from the delamination tip arrived at $t = 0.9088$ ms (marked as $*$) is shown. The results from SFEM and FEM match well within the zoomed window. Note that the analysis actually shows the high frequency pulse propagation in a finite body. In SFEM, to avoid the numerical error due to window distortion during inverse FFT, a small amount of damping $\eta$ is introduced in the wavenumbers as $k_j \leftarrow k_j(1 - i\eta)$, $\eta = 1 \times 10^{-3}$. A snap of the deformed triangular FE mesh at $t = 0.84$ ms is shown in Fig. 13. The relative slip between the delaminated faces can be seen in the snap. However, the assumption that this slip is frictionless may lead to erroneous prediction when delamination length is large. Such effect can be included using the model discussed in Section 3.3.

So far, the the comparative study from Fig. 12 shows the validity of the model when excited by single frequency tone-burst signal. The performance under broadband impact type loading (Fig. 7) is studied next. For the same beam configuration with single delamination as considered earlier, the transverse velocity history and the displacement spectrum at the cantilever tip mid-plane are shown in Fig. 14(a) and (b)

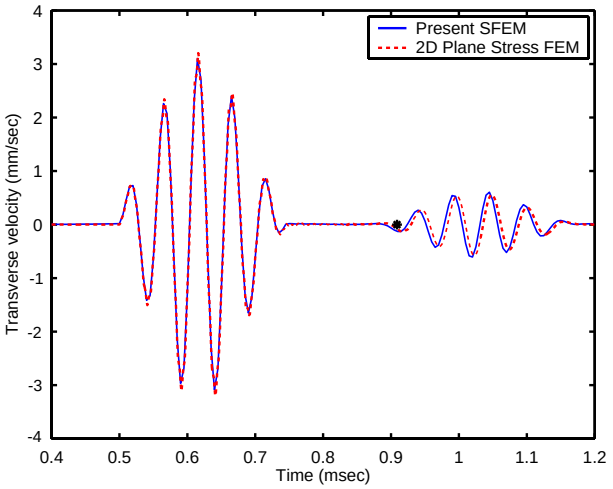


Fig. 12. Comparison of velocity history obtained from the present SFEM and a 2D plane stress FEM at the free end of a graphite-epoxy unidirectional composite cantilever beam with single mid-plane delamination. Arrival of the first reflection from the delamination tip is shown by the $*$ mark.

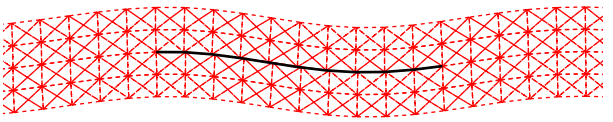

Fig. 13. Snap of the deformed FE mesh taken at the region of the delamination at $t = 0.84$ ms. The nodal displacements are magnified by $10^5$ times.

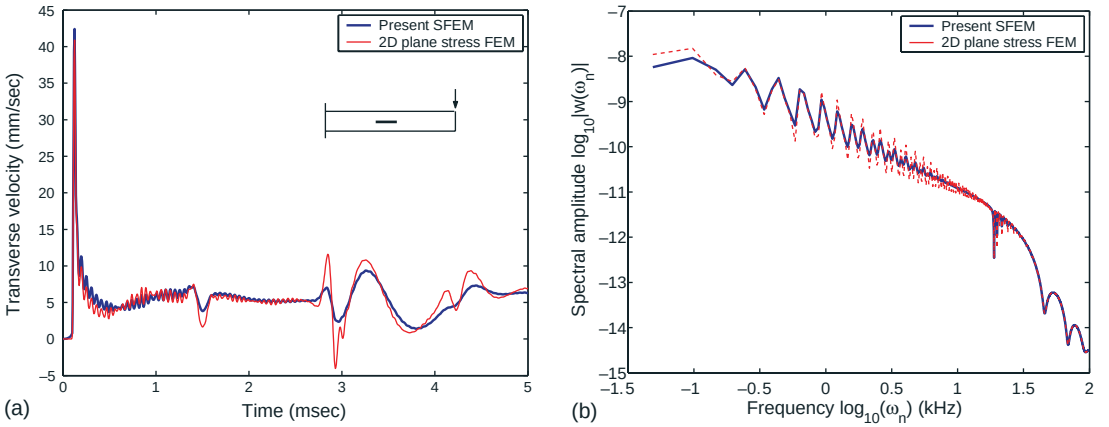


Fig. 14. Comparison of (a) transverse velocity history and (b) transverse displacement spectrum obtained from the present SFEM and the 2D plane stress FEM at the free end of a graphite-epoxy unidirectional composite cantilever beam with single mid-plane delamination.

respectively. The first arrival of the scattered wave from the delamination as well as the resonance behaviour matches well with the FEM. $\eta = 1 \times 10^{-3}$ is is used in SFEM as discussed earlier. Due to this damping, little amount of decay in the velocity response at latter time can be seen. However, the nature of the peaks are accurately captured in SFEM. Next, we consider the same cantilever beam with two mid-span delamination, each of length 50 mm placed at $z = \pm 4$ mm. Under the broadband loading (Fig. 7) applied at the cantilever tip, the response of this delaminated beam is shown in Fig. 15. Here also, similar trends can be observed in the velocity history and the displacement spectrum at the cantilever tip mid-plane. The overall performance shows acceptable accuracy of the present SFEM.

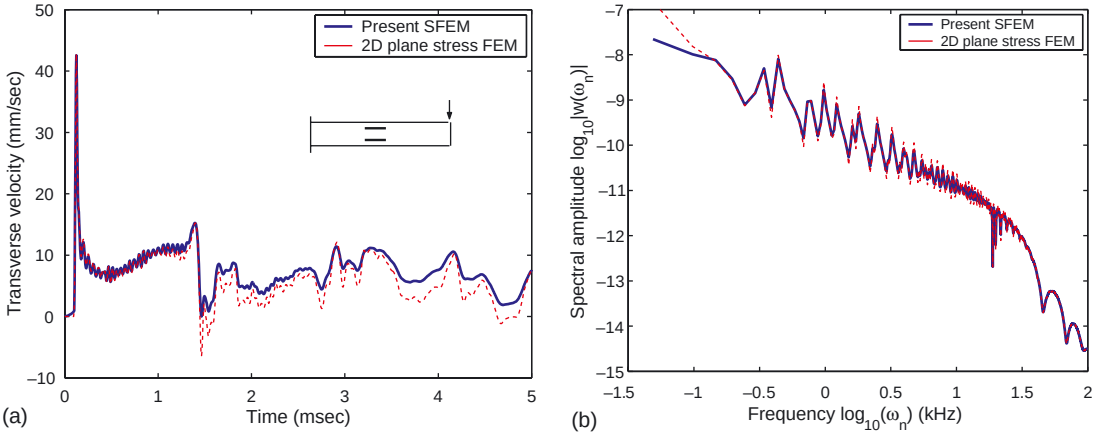


Fig. 15. Comparison of (a) transverse velocity history and (b) transverse displacement spectrum obtained from the present SFEM and the 2D plane stress FEM at the free end of a graphite-epoxy unidirectional composite cantilever beam with two symmetric delaminations at the mid-span.

#### 6.2.1. Computational efficiency of SFEM compared to FEM

It can be noted that the updated system equation (Eq. (33)) is directly solved at each FFT sampling frequency $\omega_n$, $n = 1, \ldots, N$. Since the system size in the present SFEM depends only on the number of sub-laminates and base-laminates and not on the actual length or thickness of the delaminated beam, it is very small. For example, for a beam with single delamination somewhere in the mid-span, we need maximum four waveguide elements. So, the system size can increase up to (48×48) considering 6 DOF/node. This internally constrained system is formed at each sampling frequency $\omega_n$ from the wavenumbers $k_j$ in the shape function and is solved directly. Hence, the main computational cost is in the element formulation only (as seen in the matrix manipulations). Whereas, for conventional FEM, the element size is limited by the smallest wavelength of propagation and the system size increases for increasing span and depth of the beam. For example, if the span of the beam whose existing FEM system size is $(n \times m)$, where $m$ is the bandwidth and $n$ is the number of DOF, and the span is increased by length $l_1$, then the system size will increase to $(n' \times m)$, where $n' \approx n + l_1(n_h + 1)n_d/\Delta l$, $\Delta l \approx \lambda/5$, $\lambda$ is the smallest wavelength of propagating waves, $n_h$ is the number of elements across the beam depth and $n_d$ is the number of DOF/node. Now, such large FE system is to be solved at each time step over the time window of observation while adopting a particular time integration scheme. The time step again has to comply with the high frequency nature of the excitation and is generally of the order of μm for the type of problem considered in the present paper. Obviously, the conventional FEM will be always slower and will need more memory compared to SFEM. The computational costs are given in Table 1 for the first comparative study reported in Section 6.2, which shows nearly three times higher memory requirement and two order higher computation time for FEM. Also, for the other two comparative studies, the costs remain of the same order since problem geometry in FEM and the frequency band width of analysis in SFEM remains unchanged.

### 6.3. Wave scattering due to single delamination

A graphite-epoxy unidirectional composite cantilever beam with single mid-plane delamination is considered as shown in Fig. 16. The objective here is to estimate the effect of wave scattering from the delamination tip due to different sizes $L_d$ of the mid-plane delamination. A broadband load of duration

Table 1
Computational costs while using standard FEM and the present SFEM

| | Total CPU time (s) | Memory (MB) | System size |
|---|---|---|---|
| FEM | 365.6 | 3.364 | (2898×28) |
| SFEM | 9.2 | 1.342 | (42×42) |

Computation is performed on a IBM RS/6000 high performance computer.

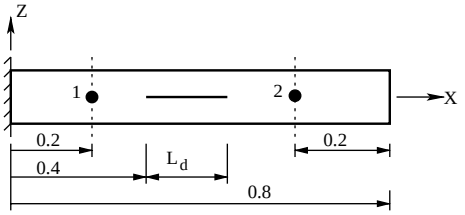


Fig. 16. A cantilever beam with single mid-plane delamination of length $L_d$. Nodal locations 1 and 2 for estimation of spectral power is shown. All dimensions are in m.

50 μs and dominant frequency content up to 40 kHz as shown in Fig. 7 is applied at the tip of the cantilever. Two measurement nodes 1 and 2 shown in Fig. 16 are used to compute the scattered power $\Delta$ (Eq. (40)) at low frequency, medium frequency and high frequency bands. For delamination lengths $L_d = 1$ cm and $L_d = 5$ cm, the spectra of scattered power are shown in Fig. 17 over a frequency range of 100 kHz. Higher amount of scattering due to 5 cm long delamination can be seen from this figure. Next, the feasibility of using the scattered power for characterizing the severity of the delamination configuration is studied. For this purpose, the delamination length $L_d$ is varied from 1 to 10 cm in steps of 0.5 cm. The scattered power at low frequency, medium frequency and high frequency bands are shown in Fig. 18. From this figure it is clear that the effect of small delaminations did not influence the energy transmission at low frequency and

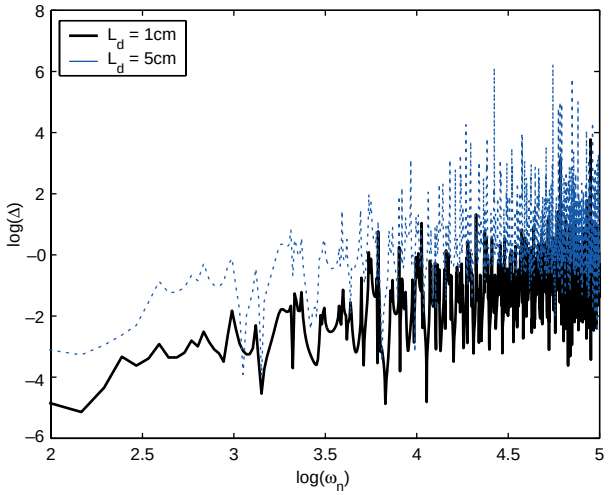


Fig. 17. Spectrum of scattered power due to delaminations of length 1 and 5 cm.

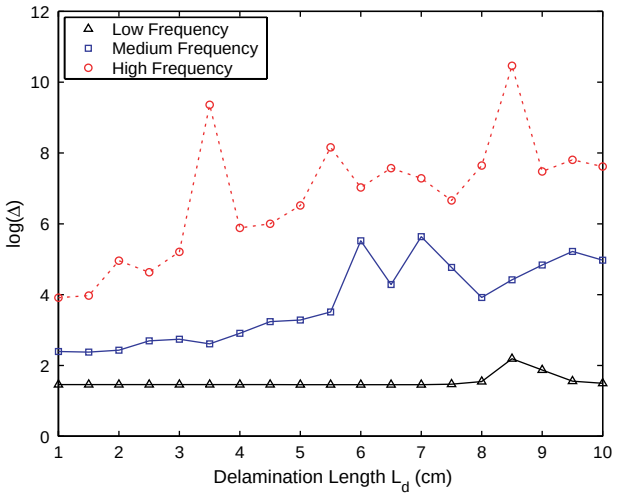


Fig. 18. Scattered power at low frequency (1 Hz–1 kHz), medium frequency (1–10 kHz) and high frequency (10–100 kHz) bands for varying length of single delamination.

medium frequency bands. For increasing length of delamination, the order of scattered power increases almost linearly at medium frequency band. Although the figure shows sudden jumps in the order of scattered power at medium and high frequency bands, the mean levels have steady increases for increasing size of delamination.

### 6.4. Wave scattering due to length-wise multiple delaminations

Here we consider length-wise multiple delaminations in the same graphite-epoxy cantilever beam as considered earlier. Fig. 19 shows the beam with three mid-plane delaminations of same length. The broadband transverse load (Fig. 7) is applied at the cantilever tip. The location of the measurement nodes 1 and 2 used to compute the scattered power measure $\Delta$ is shown in Fig. 7. In the numerical simulations, we consider three different cases containing one, two and three delaminations from the left side, respectively. Fig. 20 shows the spectrum of scattered power due to one delamination and three delaminations at high frequency band. Very little differences in the spectrum are seen from the figure. Fig. 21 shows the comparison of the three cases in low frequency, medium frequency and high frequency bands. It can be seen from this figure that increasing number of mid-plane delamination of size as considered in the simulation is less likely to alter the power flow significantly at low frequency band. Change in the order of scattered power at medium frequency band is linearly increasing with increasing number of delaminations, whereas significant change is seen at the high frequency bands.

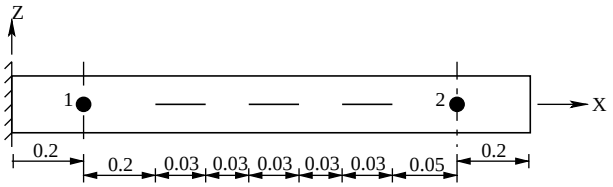


Fig. 19. A cantilever beam with length-wise multiple delaminations. Nodal locations 1 and 2 for estimation of spectral power is shown. All dimensions are in m.

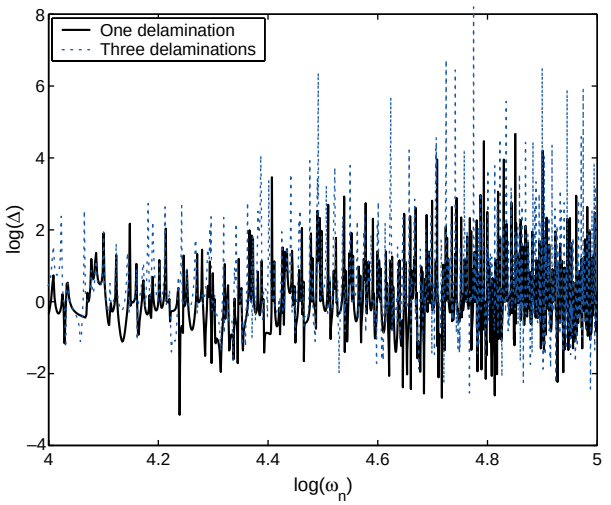


Fig. 20. Spectrum of scattered power at the high frequency band due to length-wise increasing number of delaminations.

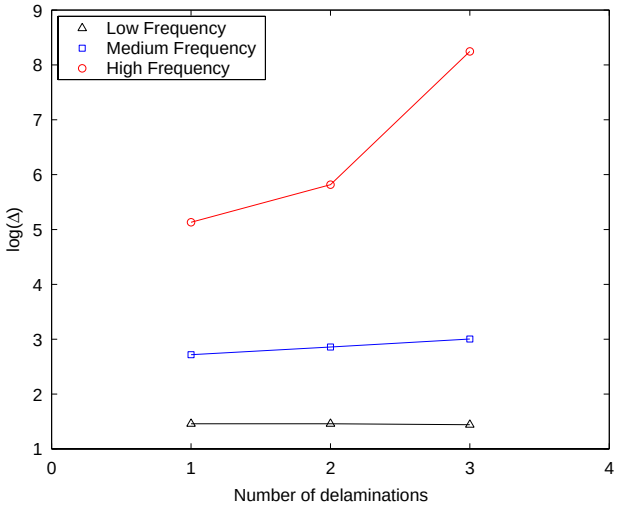


Fig. 21. Scattered power at low frequency (1 Hz–1 kHz), medium frequency (1–10 kHz) and high frequency (10–100 kHz) bands for length-wise increasing number of delaminations.

### 6.5. Wave scattering due to depth-wise multiple delaminations

Impact type loading on laminated composite structures may often cause depth-wise multiple delamination growing from the face opposite to the loading face. That is, at the bottom most interlaminar region, the size of delamination can be expected to be larger due higher interlaminar stress gradient. When, such damage has occurred, it is essential to monitor the load carrying capacity of the damaged structures, possibly using diagnostic wave measurements. Fig. 22 shows a configuration with three delaminations with progressively increasing size towards the bottom face of the unidirectional graphite-epoxy composite cantilever beam as considered in the earlier studies. In the numerical simulations we consider three cases considering one, two and three delaminations from the bottom face, respectively. The location of measurement nodes 1 and 2 for computation of scattered power is shown in Fig. 22. Fig. 23 shows the spectrum of scattered power for one and three delaminations at medium and high frequency bands. Fig. 24 shows the scattered power measure at low frequency, medium frequency and high frequency bands. It can be seen that at medium frequency band, the configuration with three delaminations creates lesser scattering than the configuration with two bottom most delaminations, which makes the direct correlation difficult. This can be attributed to the shift in the peaks as well as appearance of several additional peaks due to modification in structural discontinuities as was observed in the context of variation of delamination length (Fig. 18).

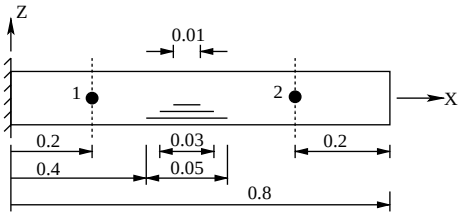


Fig. 22. A cantilever beam with depth-wise multiple delaminations. Location of the nodes 1 and 2 for estimation of spectral power is shown. All dimensions are in m.

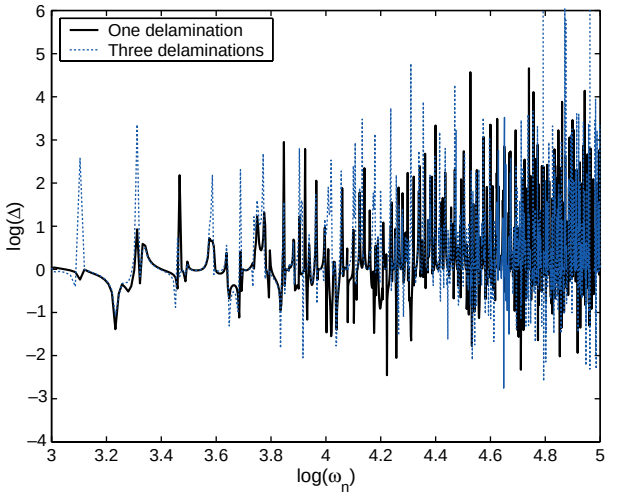


Fig. 23. Spectrum of scattered power at the medium frequency and high frequency bands due to depth-wise increasing number of delaminations.

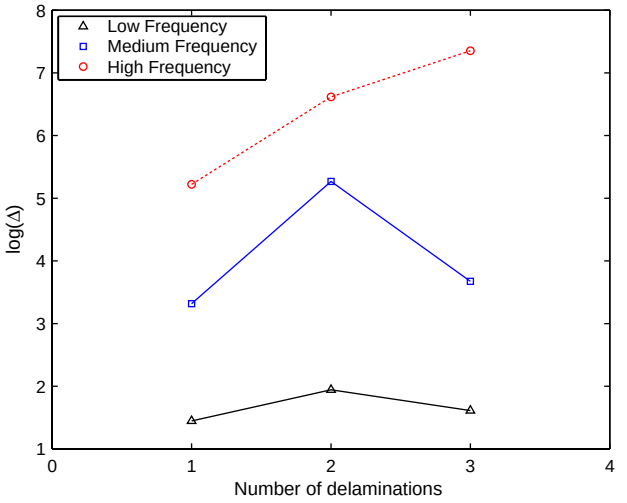


Fig. 24. Scattered power at low frequency (1 Hz–1 kHz), medium frequency (1–10 kHz) and high frequency (10–100 kHz) bands for depth-wise increasing number of delaminations.

However, the high frequency band provides a good correlation for increasing number of delaminations as seen in Fig. 24.

### *6.6. Wave scattering due to strip inclusion*

#### *6.6.1. Power flow in a semi-infinite strip inclusions with bounded media: effect of change in the material properties*

Here we study the effect of strip inclusion in laminated composite beams. Modeling of such inclusion and associated wave scattering effect is simplified using the constrained interfaces at the end of the strip

inclusions and hence by considering it as a debonded sub-laminate with different material property and bounded in viscoelastic medium (see Section 3.3) as discussed in the context of SFEM.

In laminated composite, the undelaminated interlaminar region and the delaminated surfaces are exposed to friction contact due to presence of lose fibers and matrix grain boundaries. Similarly, any foreign material system such as electronic chips, MEMS devices, embedded sensors and actuators etc. also experience dislocation from the host structures through surrounding interfaces. Although, the model presented in this papers accounts for the viscoelastic behaviour of such dislocation, only the effect of friction contact (distributed spring stiffness $K_x$ and $K_z$) are consider in the following simulations. Propagation of longitudinal and flexural waves in presence of such distributed spring stiffness are studied first. For this purpose, a semi-infinite unidirectional graphite-epoxy sub-laminate constrained by distributed spring stiffness $K_x$ and $K_z$ at the top and bottom surfaces is considered as shown in Fig. 25. The base-laminate 'A' (thickness 1.6 mm), the top and bottom sub-laminates 'B' and 'C' (thickness 6 mm each), the strip inclusion 'D' (thickness 4 mm) and the distributed media 'E' (of negligible thickness at the interlaminar region) modeled using spring stiffness ($K_x$, $K_z$) is shown in the figure. Reflection and transmission of waves propagating through the base-laminate 'A' occur at the vertical interface. The transmitted waves when propagate through the strip inclusion 'D' interact with the distributed spring in longitudinal and transverse motion. To study this behaviour, we apply a broadband load (shown in Fig. 7) longitudinally at the left end of 'D', which is semi-infinite at the other end. Fig. 26 shows the propagation of longitudinal waves as they travel from the interface at the left end to the right end. $K_x = 1 \times 10^7$ N/m and $k_j \leftarrow k_j(1 - i\eta)$, $\eta = 1 \times 10^{-3}$ is used. Note the non-dispersive nature of the longitudinal wave after the incidence (the initial peak). At increasing

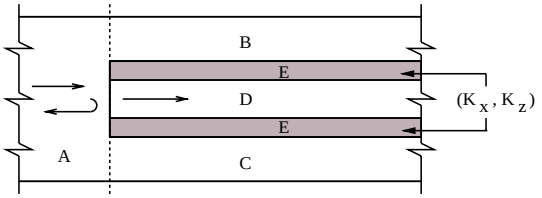


Fig. 25. Strip inclusion bounded in distributed spring in a laminated composite semi-infinite beam.

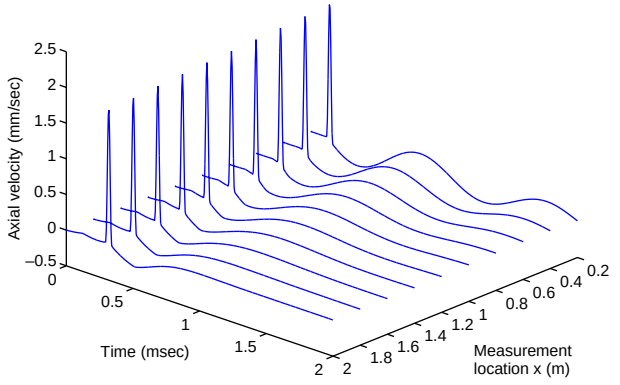


Fig. 26. Propagation of longitudinal wave in a graphite-epoxy unidirectional composite semi-infinite beam bounded in distributed uniform spring stiffness $K_x = 1 \times 10^7$ N/m at the top and bottom surfaces.

distance from the interface, this effect dies down. For varying spring stiffness $k_x$, the spectral power $\widehat{P}$ (given in Eq. (36)) at $x = 0.4$ m away from the left end is shown in Fig. 27. It can be seen from this figure that for increasing values of $K_x$, additional peaks appear from low frequency to high frequency bands. Interestingly, the number of these peaks are more in the imaginary part of spectral power compared to real part of spectral power. This can be attributed to the the fact that all the incident energy is transmitted from the left end to the right end, apart from the small amount of spatial loss due to presence of the damping factor in

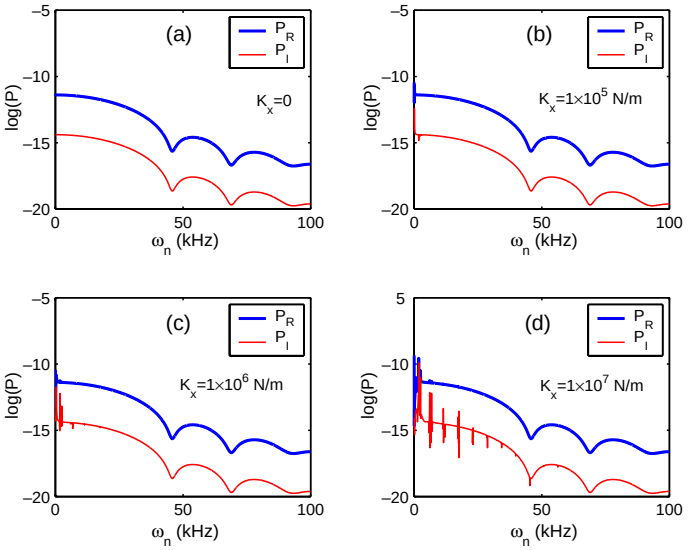


Fig. 27. Change in spectral power due to variation in distributed spring stiffness $K_x$ in propagation of longitudinal wave in graphite-epoxy unidirectional composite semi-infinite beam bounded in distributed uniform spring stiffness. Measurement location is $x = 0.4$ m.

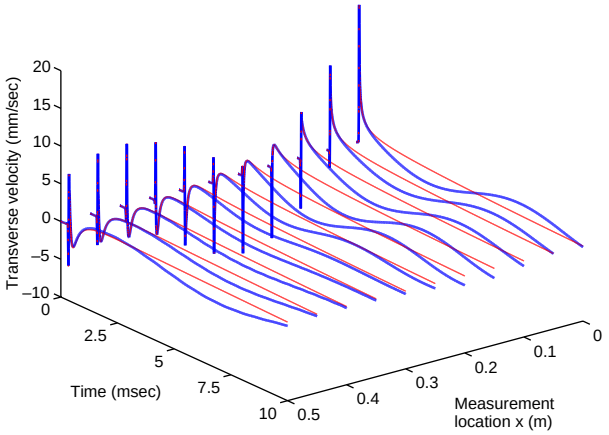


Fig. 28. Propagation of flexural wave in a graphite-epoxy unidirectional composite semi-infinite beam bounded in distributed uniform spring stiffness $K_z = 1 \times 10^5$ N/m (shown with thick solid lines) at the top and bottom surfaces. The thin solid lines show the responses for $K_z = 0$.

wavenumber $\eta$. Hence the power level, which is governed by the real part remains almost unchanged. Only significant change appear in the imaginary part of spectral power, which carries the phase information.

Next the same broadband load (Fig. 7) is applied in transverse direction at the left end of 'D'. The propagation of flexural waves is shown in Fig. 28. The incident wave amplitude changes due to dispersive nature of the flexural and shear modes, which is unaltered by the distributed spring stiffness $K_z$. However, at a later time, the additional waves of smaller amplitude and low phase modulation appear, which is otherwise absent when $K_z = 0$. For different order of magnitude of $K_z$, the spectral power at $x = 0.1$ m away from the left end is shown in Fig. 29. Unlike the case of longitudinal waves in Fig. 27, here the power flow is almost unaltered for $K_z$ up to $1 \times 10^7$ N/m. It can be observed that for $K_z = 1 \times 10^9$ N/m, the real real part of spectral power has decreased within the range of loading frequency 50 kHz, and additional peaks have appeared in the imaginary part of spectral power. Such effect can be attributed to very high spring stiffness, which actually tends to form few stop-bands by blocking the energy transmission at low and medium frequencies.

### 6.6.2. *Effect of change in the material properties of a strip inclusion*

To study the effect of the change in material properties, especially stiffness of the strip inclusion, the same graphite-epoxy unidirectional cantilever beam with a 5 cm long and 4 mm thick strip inclusion is considered as shown in Fig. 30. Similar analysis can also be applied while monitoring the health of composite beam structures with degraded material properties at sub-laminate level. For an assumed change or degradation in the elastic moduli as

$$\overline{\mathbf{C}}' = \boldsymbol{\alpha}\overline{\mathbf{C}}, \tag{41}$$

where, $\overline{\mathbf{C}}'$ is the modified elasticity matrix for composite, $\overline{\mathbf{C}}$ is the original elasticity matrix defined in Eq. (2) and $\boldsymbol{\alpha}$ is a matrix of degradation factors for simplicity. In such a case, the wavenumbers $k_j$ for the sub-laminate waveguides with degraded material properties also change following Eq. (10). Hence,

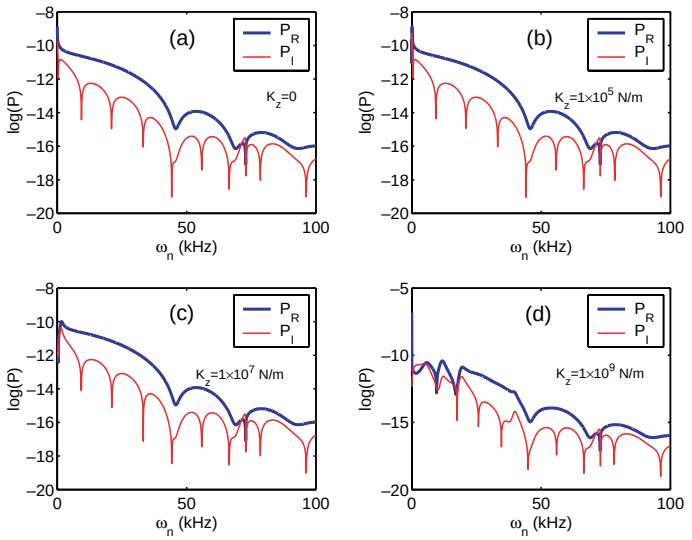


Fig. 29. Change in spectral power due to variation in distributed spring stiffness $K_z$ in propagation of flexural wave in graphite-epoxy unidirectional composite semi-infinite beam bounded in distributed uniform spring stiffness. Measurement location is $x = 0.1$ m.

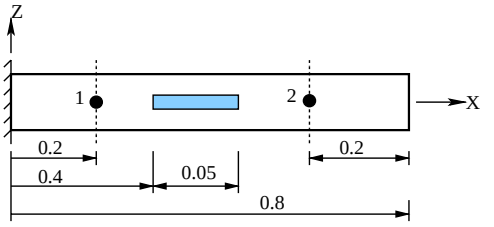


Fig. 30. A graphite-epoxy cantilever beam with a strip inclusion. Location of the nodes 1 and 2 for estimation of spectral power is shown. All dimensions are in m.

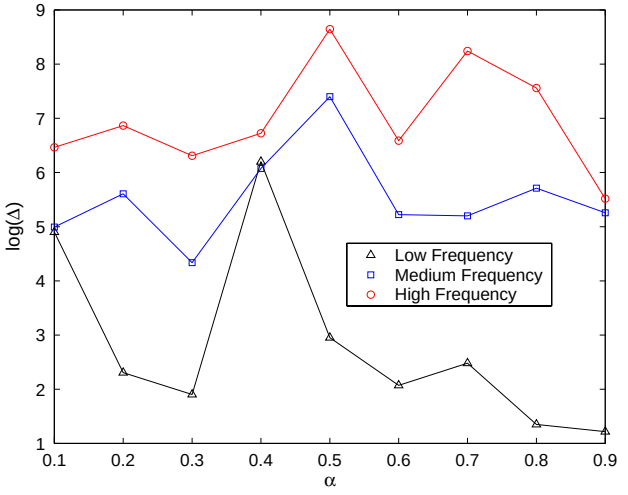


Fig. 31. Scattered power at low frequency (1 Hz–1 kHz), medium frequency (1 kHz–10 kHz) and high frequency (10 kHz–100 kHz) bands for different material stiffnesses of a strip inclusion.

the amount of scattering at the interfaces as well as the propagation of individual wave components in individual waveguides also change. In the present numerical simulations, we assume $K_x = 0$ and $K_z = 0$ and $\alpha$ is assumed same (scalar) for all the elastic moduli. Fig. 31 shows the scattered power measure at low frequency, medium frequency and high frequency bands for varying $\alpha$. From the results, a direct correlation becomes difficult especially at the medium and high frequency bands. At the low frequency band, however, significant order change in the scattered power for $\alpha = 0.4$ can be seen for which the scattered power is shown over frequency axis in Fig. 32 in comparison with $\alpha = 0.9$. The spectrum shows significant change in the peaks at low frequency that has produced such high level of scattering for $\alpha = 0.4$. Similar inference can also be drawn from the appearance of the peaks at medium and high frequency bands for $\alpha = 0.5$. The presence of wave scattering from the fixed and free ends of the cantilever also interact with the scattered waves from the interface alone and amplify the amplitude of the waves trapped between the two interfaces, the fixed and free ends of the cantilever. These higher wave amplitudes contribute in higher level of scattered power compared to single or multiple delaminations (in Figs. 18, 21 and 24) as can be seen in Fig. 32.

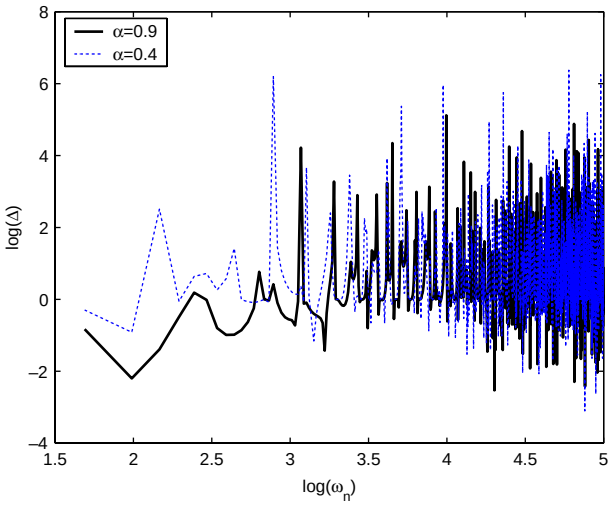


Fig. 32. Spectrum of scattered power due to 10% ($\alpha = 0.9$) and 60% ($\alpha = 0.4$) degradation in the material stiffness.

## 7. Conclusions

A spectral finite element model for coupled wave propagation in laminated composite beams with general ply stacking sequence has been developed and used to analyze the effect of single delamination of varying size, length-wise multiple delaminations, depth-wise multiple delaminations and finally the effect of wave scattering in strip inclusion with material degradation. A compact matrix methodology to obtain the numerical solution of coupled dispersion equation in wavenumber space is reported. Also, an exact shape function matrix, an exact dynamic stiffness matrix and a dynamically consistent force vector to handle distributed viscoelastic bounded media at the interlaminar or delaminated region are derived. A sub-laminate-wise constant shear kinematics model using multi-point constraints on displacements and forces is used to model the interface between the base-laminates and the sub-laminates or inclusions. The concept of spectral power flow is employed to derive a measure of scattered power, which is then employed to quantify the effect of parametric variation, such as varying length of a single delamination, the effect of length-wise and depth-wise multiple delaminations, and material degradation of a debonded strip inclusion. The results show that the derived scattered power can be used effectively to identify the severity of different types of damage and inclusions in terms of frequency domain power flow over different frequency bands and hence the energy transmission capacity of the structure. Also, efficient modeling in the framework of SFEM and FFT based pre- and post-processing can be employed in conjunction with actual signal measurement to develop strategies in integrated structural health monitoring softwares and systems. Although the kinematics of the sub-laminates has been incorporated using constraints in the present SFEM, there are certain limitations of the application of the model, where the localized effect, such as delamination growth and instability are important factors to be considered. For such local analysis, appropriate enrichment of spectral shape function or use of a local finite element mesh at the region of crack front may be possible and is an open areas of research.

## References

Barbero, E.J., Reddy, J.N., 1991. Modeling of delamination in composite laminates using a layer-wise plate theory. International Journal of Solids and Structures 28, 373–388.

Bent, A., Hagood, N.W., Rodgers, J.P., 1995. Anisotropic actuation with piezoelectric composites. Journal of Intelligent Material Systems and Structures 6 (3), 338–349.

Brennan, M.J., Elliott, S.J., Pinnington, R.J., 1997. The dynamic coupling between piezoceramic actuators and a beam. Journal of Acoustical Society of America 102 (4), 1931–1942.

Cai, C., Liu, G.R., Lam, K.Y., 2001. A technique for modelling multiple piezoelectric layers. Smart Materials and Structures 10, 689–694.

Castro, C., Zuazua, E., 1998. Boundary controllability of a hybrid system consisting in two flexible beams connected by a point mass. SIAM Journal on Control and Optimization 36, 1576–1595.

Chakraborty, A., Mahapatra, D.R., Gopalakrishnan, S., 2001. Finite element analysis of free vibration and wave propagation in asymmetric composite beams with structural discontinuities. Composite Structures 10, 1046–1058.

Clark, R.L., Saunders, W.R., Gribbs, G.P., 1998. Adaptive Structures. Wiley, NY.

Coats, T.W., Harris, C.E., 1995. Experimental verification of a progressive damage model for IM7/5260 laminates subjected to tension–tension fatigue. Journal of Composite Materials 29 (3), 280–305.

Cook, R.D., Malkus, D.S., Plesha, M.E., 1989. Concepts and Applications of Finite Element Analysis, Constraints. John Wiley & Sons, Inc. (Chapter 9).

Cowper, G.R., 1968. On the accuracy of Timoshenko beam theory. ASCE Journal of Applied Mechanics 94, 1447–1453.

Doyle, J.F., 1995. Detection of size and location of transverse crack in beams. Experimental Mechanics 35, 272–280.

Doyle, J.F., 1997. Wave Propagation in Structures. Springer-Verlag, NY.

Geubelle, P.H., Rice, J.R., 1995. A spectral method for three-dimensional elastodynamic fracture problems. Journal of Mechanics and Physics of Solids 43 (11), 1791–1824.

Gopalakrishnan, S., Doyle, J.F., 1995. Spectral super elements for wave propagation in structures with local non-uniformities. Computer Methods in Applied Mechanics and Engineering 121, 77–90.

Heschel, M., Kuhmann, J.F., Bouwstra, S., Amskov, M., 1998. Stacking technology for a space constrained microsystem. Journal of Intelligent Material Systems and Structures 9, 749–754.

Howard, C.Q., Snyder, S.D., Hansen, C.H., 2000. Calculation of vibratory power transmission for use in active vibration control. Journal of Sound and Vibration 233 (4), 573–585.

Kessler, S.S., Spearing, S.M., Soutis, C., 2002. Damage detection in composite materials using Lamb wave methods. Smart Materials and Structures 11, 269–278.

Kouchakzadeh, M.A., Sekine, H., 2000. Compressive buckling analysis of rectangular composite laminates containing multiple delaminations. Composite Structures 50, 249–255.

Lakshmanan, K.A., Pines, D.J., 1998. Damage identification of chordwise crack size and location in uncoupled composite rotorcraft flexbeams. Journal of Intelligent Material Systems and Structures 9, 146–155.

Lee, J., 2000. Free vibration analysis of delaminated composite beams. Computers and Structures 74, 121–129.

Lee, J., Gurdal, Z., Griffin Jr., H., 1993. Layer-wise approach for the bifurcation problem in laminated composites with delaminations. AIAA Journal 31 (2), 331–338.

Lee, U., Kim, J., 2000. Determination of nonideal beam boundary conditions: a spectral element approach. AIAA Journal 38 (2), 309–316.

Lin, X., Yuan, F.G., 2001. Diagnostic Lamb waves in an integrated piezoelectric sensor/actuator plate: analytical and experimental studies. Smart Materials and Structures 10, 907–913.

Liu, G.R., 2002. A combined finite element/strip element method for analyzing elastic wave scattering by cracks and inclusions in laminates. Computational Mechanics 28, 76–82.

Liu, G.R., Achenbach, J.D., 1995. Strip element method to analyze wave scattering by cracks in anisotropic laminated plates. Journal of Applied Mechanics 62, 607–613.

Luo, H., Hanagud, S., 2000. Dynamics of delaminated beams. International Journal of Solids and Structures 37, 1501–1519.

Mahapatra, D.R., Gopalakrishnan, S., 2003. A spectral finite element model for analysis of axial–flexural–shear coupled wave propagation in laminated composite beams. Composite Structures 59 (1), 67–88.

Mahapatra, D.R., Gopalakrishnan, S., Sankar, T.S., 2000. Spectral-element-based solutions for wave propagation analysis of multiply connected laminated composite beams. Journal of Sound and Vibration 237 (5), 819–836.

Mahapatra, D.R., Gopalakrishnan, S., Balachandran, B., 2001a. Active feedback control of multiple waves in helicopter gearbox support struts. Smart Materials and Structures 10, 1046–1058.

Mahapatra, D.R., Gopalakrishnan, S., Sankar, T.S., 2001b. Scattering and transmission of mixed-mode waves in delaminated thick composite beams. ASME Design Engineering Technical Conference, 18th Biennial Conference on Vibration and Noise, Pittsburgh, Pennsylvania, USA, Sept. 9–12. Paper no. DETC01-VIB-21543.

Nag, A., Mahapatra, D.R., Gopalakrishnan, S., 2002. Identification of delamination in a composite beam using a damaged spectral element. Structural Health Monitoring 1 (1), 105–126.

Nag, A., Roy Mahapatra, D., Gopalakrishnan, S., Sankar, T.S., 2003. A spectral finite element with embedded delamination for modeling of wave scattering in composite beams. Composite Science and Technology 63, 2187–2200.

Pagano, N.J., 1989. Interlaminar Response of Composite Materials. In: Composite Materials Series, 5. Elsevier.

Park, G., Cudney, H.H., Inman, D.J., 2000. An Integrated monitoring technique using structural impedence sensors. Journal of Intelligent Material Systems and Structures 11, 448–455.

Purekar, A.S., Pines, D.J., 2000. Detecting damage in non-uniform beams using the dereververated transfer function response. Smart Materials and Structures 9, 429–444.

Reddy, J.N., 1997. Mechanics of Laminated Composite Plates. CRC Press, USA.

Sankar, B.V., Zhu, H., 2000. The effect of stitching on the low-velocity impact response of delaminated composite beams. Composite Science and Technology 60, 2681–2691.

Seeling, J.M., Hoppmann, W.H.H., 1964. Impact on an elastically connected double beam system. Journal of Applied Mechanics 31, 621–626.

Senthil, S.V., Batra, R.C., 2001. Exact solution for the cylindrical bending of laminated plates with embedded piezoelectric shear actuators. Smart Materials and Structures 10, 240–251.

Tanaka, N., Kikushima, Y., 1999. Optimal vibration feedback control of an Euler–Bernoulli beam: toward realization of the active sink method. Journal of Vibration and Acoustics 121, 174–182.

Tong, L., Sun, D., Atluri, S.N., 2001. Sensing and actuating behaviours of piezoelectric layers with debonding in smart beams. Smart Materials and Structures 10 (4), 713–723.

Tsai, J.L., Guo, C., Sun, C.T., 2001. Dynamic delamination fracture toughness in unidirectional polymer composites. Composite Science and Technology 61, 87–94.

Tupper, H.T., 2000. Smart structures and materials 2000: damping and isolation. In: Proceedings of SPIE, vol. 3989.

Valdez, S.H.D., Soutis, C., 2001. A structural health monitoring system for laminated composites. ASME Design Engineering Technical Conference, Proc. of 18th Biennial Conference on Vibration and Noise, Pittsburgh, Pennsylvania, USA.

Xi, Z.C, Liu, G.R., Lam, K.Y., Shang, H.M., 2000. A strip-element method for analyzing wave scattering by a crack in a fluid-filled composite cylindrical shell. Composite Science and Technology 60, 1985–1996.